NLO thermal corrections to dark matter annihilation cross sections: a novel approach

Prabhat Butola[*1,2], D. Indumathi[†1,2], and Pritam Sen[‡3]

[1]Homi Bhabha National Institute, Mumbai, India
[2]Institute of Mathematical Sciences, Chennai, India
[3]Tata Institute of Fundamental Research, Mumbai, India

April 25, 2024

Abstract

The dark matter relic density has been increasingly accurately measured by successive generations of experiments. The Boltzmann equation determines the yields using the dark matter annihilation cross section as one of the inputs; the accurate computation of the latter including thermal contributions thus assumes importance. We report here the next-to-leading order (NLO) thermal corrections to the cross sections for (Majorana) dark matter annihilation to standard model fermions: $\chi\chi \to f\bar{f}$, via charged scalars. We use a novel approach, utilising the technique of Grammer and Yennie, extended to thermal field theories, where the cancellation of soft infra-red divergences occurs naturally. We present the NLO thermal cross sections in full detail for both the relativistic case as well as in the non-relativistic limit. Our independent calculation verifies earlier results where the leading contribution at order $\mathcal{O}(T^2)$ was shown to be proportional to the square of the fermion mass in the non-relativistic limit, just as at leading order. We find that the $\mathcal{O}(T^4)$ contributions have the same dependence on the fermion mass as well.

Keywords: Thermal field theory, Dark Matter annihilation, NLO cross section

1 Introduction

Evidence for the presence of dark matter (DM) in our Universe arises from several observations, primarily due to its interaction with standard model particles via the gravitational channel [1]. Evidence for the existence of dark matter includes its effect in gravitational lensing, structure formation and its presence is a necessity for stability of rotating galaxies; various experiments have set limits or constrained various properties of dark matter [2–7] via whole-sky or galactic observations.

---

[*]prabhatb@imsc.res.in,
[†]indu@imsc.res.in,
[‡]pritam.sen@tifr.res.in,

Cosmic microwave background radiation is sensitive to the baryonic, dark and the total matter densities respectively, through the height of the peaks in its power spectrum. The relic abundance of dark matter (DM) is encoded in its relic density, currently measured to be $\Omega_c h^2 = 0.1200 \pm 0.0012$ by the PLANCK collaboration [2], where h is the reduced Hubble constant, $h = H_0/100$. This is higher than the abundance of baryonic matter and lower than the share of dark energy in the energy density of our Universe.

Unfortunately, there is as yet no direct evidence for dark matter via, for example, whole-sky searches of self-annihilation of dark matter to produce gamma rays [3], galactic surveys [4], etc. Various non-baryonic and baryonic DM candidates have been postulated [8–11] such as WIMPs, axion-like particles (ALP), neutralino dark matter, sterile neutrinos, particles in extra dimensional theories, primordial black holes, etc.; see Refs. [7, 12–16] for reviews. A large sub-set of theoretical proposals and experiments to detect them from cosmology, colliders, etc., exist; a few recent ones can be found in Refs. [17–23].

One of the popular theories of dark matter consists of a SUSY-inspired model of bino-like cold dark matter produced thermally in the Universe post-inflation. The number density of the dark matter is then determined by Boltzmann equations dependent on the interaction rate (annihilation/production of the dark matter) as well as the expansion rate of the Universe. The dark matter is in thermal, chemical and kinetic equilibrium with standard model (SM) particles until its interaction rate falls below the Hubble expansion rate [24]. In such a freeze-out mechanism for thermal production of dark matter [25–27], the DM starts decoupling from the background plasma, when the Hubble rate of expansion of our Universe became comparable to the annihilation rate of DM species via, for example, $\chi\chi \to f\overline{f}$. The temperature where DM decouples from SM particles (f), depends on the mass of DM as well as the thermally averaged annihilation cross section $\langle \sigma v_{\text{Møl}} \rangle$, and we have a range of temperature where the mass of DM can be comparable to decoupling temperature, i.e., $x \equiv m_\chi/T \sim \mathcal{O}(1)$. In this range of temperature, thermal corrections can play an important role in determining the precise relic density of dark matter. In particular, the larger the dark matter annihilation cross section, the later the DM goes out of equilibrium, leading to a lower relic density, and vice versa.

A contrasting model is when the dark matter is never in equilibrium with the SM particles; instead, the coupling of DM to SM particles is so small that the annihilation of $\chi\chi \to f\overline{f}$ can be neglected. The amount of dark matter in the Universe then keeps on increasing due to the reverse annihilation process $f\overline{f} \to \chi\chi$ until the dark matter freezes-in to the present relic density [28].

In any case, present-day determination of dark matter relic densities are becoming so precise that these cross sections must necessarily be calculated to next-to-leading order (NLO). While NLO calculations of various relevant cross sections exist [29–36], these mostly focussed on higher order *quantum corrections* to the leading cross sections in various models. It was only recently that the higher order *thermal corrections* to these cross sections have been calculated [37–39]. In particular, Beneke et al. [39] computed the thermal NLO corrections to the dark matter annihilation cross section in a bino-like model of dark matter using thermal field theory that we describe briefly below. In this model, the dark matter candidate is an $SU(2) \times U(1)$ singlet Majorana fermion χ which interacts with SM doublet fermions, $f = (f^0, f^-)^T$, via scalar partners

$\phi = (\phi^+, \phi^0)^T$ through a Yukawa interaction,

$$\mathcal{L} = -\frac{1}{4} F_{\mu\nu} F^{\mu\nu} + \overline{f} \left(i\slashed{D} - m_f \right) f + \frac{1}{2} \overline{\chi} \left(i\slashed{\partial} - m_\chi \right) \chi$$
$$+ \left(D^\mu \phi \right)^\dagger \left(D_\mu \phi \right) - m_\phi^2 \phi^\dagger \phi + \left(\lambda \overline{\chi} P_L f^- \phi^+ + \text{h.c.} \right) . \tag{1}$$

The thermal corrections to the annihilation of dark matter via $\chi\chi \to f\overline{f}$ at NLO in this model were studied in Ref. [39] where the cancellation of the infrared divergences was explicitly demonstrated. Subsequently, an all-order proof of the cancellation of infra-red divergences in such thermal field theories containing scalars and fermions interacting with photons in a heat bath at finite temperature was given in Refs. [40, 41], using a generalised Grammer and Yennie technique [42–44] although the finite remainder was not calculated. The advantage of this approach is the automatic cancellation of the soft infra-red (IR) divergences so that we can directly compute the finite remainder. The calculations are simpler because they are explicitly IR finite. Here we compute the IR-finite contributions to the annihilation cross section at NLO, using the same technique. We calculate both the $\mathcal{O}(T^2)$ and $\mathcal{O}(T^4)$ corrections both in the relativistic case and in the non-relativistic limit using this novel approach to obtain an independent calculation of the NLO thermal contributions to the annihilation cross section, and determine the contribution in the non-relativistic limit. The latter are important at freeze-out when $m_\chi/T \sim 20$. We show that the $\mathcal{O}(T^2)$ terms are proportional to the square of the fermion masses, just as for the LO cross section, a result which arises due to helicity suppression of the process due to the presence of Majorana fermions. This result was first obtained in Ref. [39] who subsequently calculated [45] the cross section for annihilation of Dirac-type dark matter particles using the Operator Product Expansion approach.

We make a careful study of the dependence of both the $\mathcal{O}(T^2)$ and $\mathcal{O}(T^4)$ corrections; the $\mathcal{O}(T^2)$ terms are indeed proportional to m_f^2 in the non-relativistic limit, while there are terms proportional to the square of the dark matter momenta p^2 in the general case, which of course are small in the non-relativistic limit. We find in addition that the leading $\mathcal{O}(T^4)$ terms are also proportional to the square of the fermion masses in the non-relativistic limit; hence it appears that helicity conservation determines this behaviour beyond the leading order as well. We discuss the general behaviour of the cross section as well as the behaviour in the non-relativistic limit; detailed expressions for the cross section are available online [46] as sets of Mathematica Notebooks.

In the next section, we highlight some key points of thermal field theory in the real time formalism. In Section 3, we present the details of the Grammer and Yennie approach which allows us to easily separate the IR-finite part of the cross section. We also discuss some technical details about the various contributions which allow us to simplify the calculation at NLO. In Section 4 we calculate the leading order cross section, which is presented for completeness. In Sections 5 and 6, we calculate the NLO cross section in two different scenarios. For both the LO and NLO calculations, we use the FeynCalc [47–49] software with Mathematica 13 [50]. We end with Discussions in Section 7.

2 Thermal field theory

We briefly review the real-time formulation of thermal field theories [51–54]. The ensemble average of an operator can be written [53] as the expectation value of time-ordered products in the thermal vacuum. The unique feature is that the integration in the

complex time plane is defined over a special path shown in Fig. 1, from an initial time, t_i to a final time, $t_i - i\beta$, where β is the inverse temperature of the heat bath, $\beta = 1/T$;. As a result, the thermal fields satisfy the periodic boundary conditions,

$$\varphi(t_0) = \pm\varphi(t_0 - i\beta) \, ,$$

where the sign $+1$ (-1) corresponds to boson (fermion) fields. The real-time axis C_1 allows for scattering to be defined while the remaining portions of the contour lead to a doubling of the fields, which can be of type-1 (the physical fields), or type-2 (the "ghost" fields), that live on C_1 and C_2 respectively.
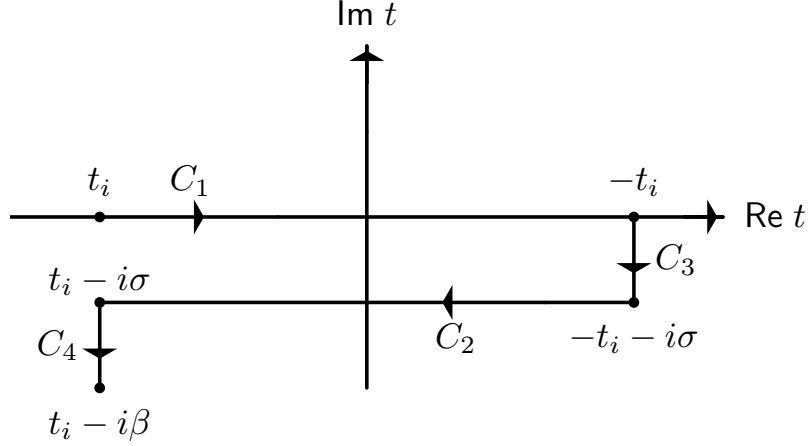

Figure 1: *The time path for real time formulation of thermal field theories in the complex t plane, where the y axis corresponds to* $\mathrm{Im}\, t = \beta$, *the inverse temperature.*

Only type-1 fields can occur on external legs [54] while fields of both types can occur on internal legs, with the off-diagonal elements of the propagator allowing for conversion of one type into another. The Feynman rules (for the propagators and vertices) for the Lagrangian density given in Eq.1 in a heat bath at finite temperature T are listed in Appendix A. We merely note here that all propagators (which are of 2×2 matrix form), can be written as the sum of two terms, one which is temperature-independent and the other which contains the explicitly thermal dependence which we call the thermal part.

3   The Grammer and Yennie approach

The application of the generalised Grammer and Yennie approach for the case of the bino-like Lagrangian described in Eq. 1 has been described in detail in Refs. [40, 41]. Here we summarise the main results for the sake of completeness, clarity and use of notation.

We use a generalised version of the Grammer and Yennie technique [42, 43] which was used for the zero temperature quantum field theory to separate the infrared (IR) divergences in the theory. The technique was extended to the case of thermal field theory, first for the case of the interaction of charged fermions with photons in thermal QED [44], and later for both charged thermal scalars and a general theory of charged scalars and fermions interacting with dark matter particles with thermal QED corrections [40, 41]. In all these instances, the all-order cancellation of infra-red (IR) divergences was shown by separating the virtual photon propagator into two parts, the

so-called K and G photons, which we define below, such that the IR divergence was completely contained in the K photon contribution and the G photon contribution was IR finite. However, as mentioned earlier, the IR-finite part was not explicitly calculated in Ref. [40] and is the goal of this work.

The Grammer and Yennie procedure is to insert a virtual photon with momentum k into a lower order graph, for (say) the process $A(p)B(q) \rightarrow C(p')$, such that the momentum q, flowing into a given vertex V, is not soft; this special vertex V is labelled as a hard vertex with respect to which the graph can be separated into a notional (initial) p_i-leg and a (final) p_f-leg. We will identify V, p_i and p_f for the dark matter annihilation diagrams of interest in the next section. The K and G parts are subsequently identified with respect to these definitions. The additional inserted photon can be soft, in which case the points of insertion will be labelled as soft vertices, and will contribute to the IR divergence of the corresponding cross section. The procedure starts with re-arranging, in its propagator term,

$$-ig^{\mu\nu} \rightarrow -i\left\{ \left[g^{\mu\nu} - b_k(p_f, p_i)\, k^\mu k^\nu \right] + \left[b_k(p_f, p_i) k^\mu k^\nu \right] \right\} ,$$
$$\equiv -i\left\{ \left[G_k^{\mu\nu} \right] + \left[K_k^{\mu\nu} \right] \right\} , \tag{2}$$

where

$$b_k(p_f, p_i) = \frac{1}{2}\left[\frac{(2p_f - k)\cdot(2p_i - k)}{((p_f - k)^2 - m^2)((p_i - k)^2 - m^2)} + (k \leftrightarrow -k) \right] , \tag{3}$$

is defined symmetrically in $k \rightarrow -k$ for the thermal case (in contrast to the original definition in Ref. [42]), and is a function of k as well as the momenta, p_f, p_i. It can then be shown that the K photon insertions contain the IR divergent pieces while the G photon contribution is IR finite.

3.1 The K photon insertion and the IR divergent piece

We briefly describe, for the sake of completeness, the separation and cancellation of IR divergences in the theory. Details are available in Refs. [40, 41]. Let us start with the example of insertion of an additional virtual photon in the lowest-order diagrams shown in Fig. 2. The key step is to specifically define a "hard vertex" V with respect to which we can identify the momenta p_f and p_i. We (arbitrarily) define this special vertex V to be the one where the momentum q' (of χ) enters. Then, a higher order diagram can be obtained by inserting a virtual photon anywhere in either of the LO diagrams shown in Fig. 2. For every such insertion, p_f (p_i) will correspond to the momentum p' or p depending on whether the final (initial) vertex of the virtual photon was inserted on the p' or p leg. Then for example, a virtual photon inserted with one vertex on the final fermion leg and one on the scalar leg (as in Diagram (1) of Fig. 4), will have a virtual photon propagator involving the term $b_k(p', p)$ since the p_f line corresponds to the p' leg, while the p_i line corresponds to the scalar leg from V to X together with the anti-fermion leg with momentum p. Thus the corresponding K and G photon insertions can be defined using Eq. 2. For the u-channel diagram, such an insertion will involve $b_k(p', p')$; see Ref. [40] for more details.

We now demonstrate the factorisation of the IR divergences in the K-photon insertions. We take the example of the case when the inserted photon has both its vertices, μ, ν, on the p' fermion line. The relevant part of the matrix element can be expressed
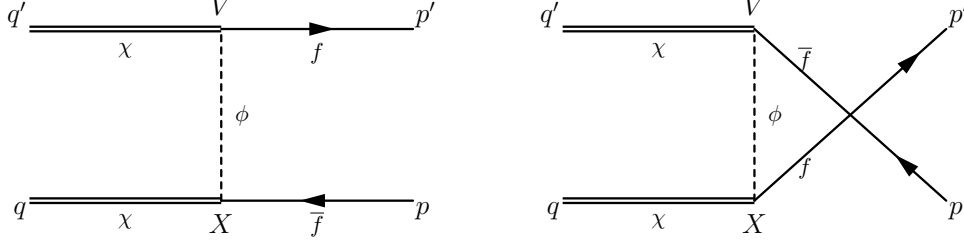
5

Figure 2: *The t-channel and u-channel dark matter annihilation processes at leading order (LO).*

as (note that there is an integration measure over the photon momentum, k)

$$M_{NLO}^{p'p',K\text{photon}} \propto b_k(p',p')k^\mu k^\nu \left[\overline{u}(p',m_f)\gamma_\mu \, \mathcal{S}_{\text{fermion}}^{t_\mu,t_\nu}(p'+k,m_f)\gamma_\nu \, \mathcal{S}_{\text{fermion}}^{t_\nu,t_V}(p',m_f)P_R \, u(q',m_\chi) \right] \cdots \, ,$$
$$= b_k(p',p') \left[\overline{u}_{p'} \, \slashed{k} \mathcal{S}_{p'+k}^{\mu,\nu} \, \slashed{k} \, \mathcal{S}_{p'}^{\nu,V} P_R \, u_{q'} \right] \cdots \, , \tag{4}$$

where the ellipsis refer to terms independent of k and we have lightened the notation for convenience in the second line, with the superscripts on $\mathcal{S}$ referring to the thermal type. The term in the square brackets can be simplified, using the identities given in Appendix A.1 as

$$[\quad] = \left[\overline{u}_{p'} \, \slashed{k} \left\{ \mathcal{S}_{p'+k}^{\mu,\nu} \, \slashed{k} \mathcal{S}_{p'}^{\nu,V} \right\} P_R \, u_{q'} \right] \, ,$$
$$= (-1)^{t_\nu+1} \left[\overline{u}_{p'} \, \slashed{k} \left\{ \mathcal{S}_{p'}^{\mu,V} \, \delta_{t_\nu,t_V} - \mathcal{S}_{p'+k}^{\mu,V} \, \delta_{t_\nu,t_\mu} \right\} P_R \, u_{q'} \right] \, ,$$
$$= (-1)^{t_\nu+1} \left[\overline{u}_{p'} \left\{ 0 - \left[(-1)^{t_\mu+1} \delta_{t_\nu,t_\mu} \right] \right\} P_R \, u_{q'} \right] \, , \tag{5}$$

where the first term vanishes since the integrand is odd in $k \to -k$ while both b_k and the measure are even under this exchange. The crucial step is seen in the second line of Eq. 5, where the Feynman identities (see Eq. A.8) are used to reduce the portions with $\slashed{k}$ insertions to a *difference* of two terms. Hence the matrix element factorises into two terms, one that is proportional to the lower order matrix element, *viz.*,

$$M_{NLO}^{p'p',K\text{photon}} \propto b_k(p',p') \, M_{LO} \, , \tag{6}$$

and the other containing the IR divergence.

3.1.1 Insertion into a general n^{th} order graph

Consider an nth order graph with n virtual/real photon vertices; for specificity, we consider higher order corrections to the t-channel diagram. When an additional virtual K-photon is inserted into this graph, there are several possible locations where the additional photon vertices can be inserted. Adding all the contributions gives differences of two terms as seen above, with, more importantly, sets of terms cancelling against each other until only one term, that is proportional to the lower order matrix element, is left.

A similar result is obtained when the photon vertices are inserted so that one vertex μ is on the p' leg and the other ν vertex is on the p leg; that is, either on the scalar line or the anti-fermion line. Here again, it turns out that the K photon contribution

6

is proportional[1] to the lower order matrix element:

$$M_{n+1}^{p'p,K\text{photon}} \propto b_k(p',p)\, M_n \;,$$ (7)

In fact, such an insertion is the sum of contributions when the second ν vertex of the virtual photon is inserted on the scalar, and when it is inserted on the anti-fermion line. These contributions separately cancel among themselves, leaving one term in the former and two in the latter. These cancel across the vertex V, leaving behind a contribution that is again proportional to the lower order graph, as seen in Eq. 7 above. In short, it is found [40] that the total matrix element due to insertion of the virtual K photon into an nth order diagram is given by

$$
\begin{aligned}
\mathcal{M}_{n+1}^{K\text{photon,tot}} &= \left[\frac{ie^2}{2} \int \frac{\mathrm{d}^4 k}{(2\pi)^4} \left\{ \delta_{t_\mu,t_1}\, \delta_{t_\nu,t_1}\, D^{t_\mu,t_\nu}(k)\, \left[b_k(p',p') + b_k(p,p) \right] \right.\right. \\
&\qquad \left.\left. + \; \delta_{t_\mu,t_V}\, \delta_{t_\nu,t_V}\, D^{t_\mu,t_\nu}(k)\, \left[-2b_k(p',p) \right] \right\} \right] \mathcal{M}_n \;, \\
&\equiv [B]\, \mathcal{M}_n \;,
\end{aligned}
$$ (8)

where the prefactor containing the IR divergence can be expressed as,

$$
\begin{aligned}
B &= \frac{ie^2}{2} \int \frac{\mathrm{d}^4 k}{(2\pi)^4}\, D^{11}(k)\, \left[b_k(p',p') - 2b_k(p',p) + b_k(p,p) \right] \;, \\
&\equiv \frac{ie^2}{2} \int \frac{\mathrm{d}^4 k}{(2\pi)^4}\, D^{11}(k)\, \left[J^2(k) \right] \;,
\end{aligned}
$$ (9)

since the thermal types of the hard/external vertices must be type-1. We see that each term is proportional to the (11) component of the photon contribution and this is crucial for achieving the cancellation between virtual and real photon insertions. When the contributions are summed over all orders in perturbation theory, the IR divergent factor B exponentiates and cancels a similar IR divergent factor arising from real soft photon insertions; for details please refer to Ref. [40].

3.1.2 Insertion of the photon into a thermal fermion line

We already know that the presence of the bosonic number operator, $n_B(|k^0|)$, makes the IR contribution to the cross section potentially IR divergent while the nature of the fermionic number operator, $n_F(|p^0|)$, results in a finite IR contribution to the cross section. In particular, we shall see below that the K-photon contribution when the additional photon is inserted into a thermal fermion (that is, when the second, temperature-dependent term in the fermionic propagator contributes; see Eq. A.3), is zero. We will use this result later in the computation of the NLO cross section of interest. In order to show this, we begin with the insertion of one of the vertices of the additional K photon on any thermal fermion line at the vertex μ, lying between vertices μ_{q+1} and μ_q; see Fig. 3.

There are now two fermion propagators, one between vertices μ_q and μ and the other between vertices μ and μ_{q+1}. The relevant part of the matrix element is given by

---

[1]Technically, a virtual photon insertion leads to the number of vertices increasing by 2; we have used the index $(n+1)$ to indicate that it is an nth order graph with an additional virtual photon.
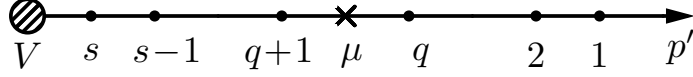
Figure 3: *Sample insertion of vertex μ of virtual photon between vertices μ_q and μ_{q+1} on the p' fermion line. The labels have been simplified ($\mu_i \to i$) for the sake of clarity. Only a portion of the diagram containing the p' leg to the right of vertex V has been shown here.*

(where we have chosen to insert into the p' fermion line for specificity),

$$M_{NLO}^{\text{thermal f},K\gamma} \propto b(p_f, p_i) k^\mu k^\nu \left[\bar{u}_{p'} \gamma_{\mu_1} \cdots \gamma_{\mu_q} \mathcal{S}_{p'+\Sigma_q}^{q,\mu} \gamma_\mu \mathcal{S}_{p'+\Sigma_q+k}^{\mu,q+1} \gamma_{\mu_{q+1}} \right] \cdots ,$$

$$= b(p_f, p_i) k^\nu \left[\bar{u}_{p'} \gamma_{\mu_1} \cdots \gamma_{\mu_q} \left\{ \mathcal{S}_{p'+\Sigma_q}^{q,\mu} \not{k} \mathcal{S}_{p'+\Sigma_q+k}^{\mu,q+1} \right\} \gamma_{\mu_{q+1}} \right] \cdots , \quad (10)$$

where the momentum flowing in the fermion line between vertices q and $(q+1)$ into which the additional photon was inserted is $p' + l_1 + \cdots + l_q \equiv p' + \Sigma_q$. The term in curly braces can be simplified using the property of the fermion propagator shown in Eq. A.3 where $\overline{S}$ is also defined:

$$\{\cdots\} = \left[(\not{p}' + \not{\Sigma}_q + m_f) \not{k} (\not{p}' + \not{\Sigma}_q + \not{k} + m_f) \right] \overline{S}_{p'+\Sigma_q}^{q,\mu} \overline{S}_{p'+\Sigma_q+k}^{\mu,q+1} ,$$

$$= \left[(2(p' + \Sigma_q) \cdot k + k^2)(\not{p}' + \not{\Sigma}_q + m_f) - ((p' + \Sigma_q)^2 - m_f^2) \not{k} \right] ,$$

$$= 0 \quad \text{for thermal fermions.} \quad (11)$$

In particular, if both the fermion propagators on either side of the K-photon insertion at the vertex μ are thermal, then both terms in Eq. 11 vanish due to the delta function terms $\delta((p' + \Sigma_q)^2 - m_f^2)$ and $\delta((p' + \Sigma_q + k)^2 - m_f^2)$ in the thermal part of the respective propagators. We will use this result in the next section when we compute the NLO cross section.

In order to show the IR divergence cancellation between virtual and real photon contributions, a similar treatment of the real photon corrections to the process is done, by separating the polarisation sums for the insertion of real photons into so-called $\widetilde{K}$ and $\widetilde{G}$ contributions:

$$\sum_{\text{pol}} \epsilon^{*,\mu}(k) \, \epsilon^\nu(k) = -g^{\mu\nu} ,$$

$$= -\left\{ \left[g^{\mu\nu} - \tilde{b}_k(p_f, p_i) k^\mu k^\nu \right] + \left[\tilde{b}_k(p_f, p_i) k^\mu k^\nu \right] \right\} , \quad (12)$$

$$\equiv -\left\{ \left[\widetilde{G}_k^{\mu\nu} \right] + \left[\widetilde{K}_k^{\mu\nu} \right] \right\} .$$

Since $k^2 = 0$ for real photons, we define,

$$\tilde{b}_k(p_f, p_i) = b_k(p_f, p_i) \Big|_{k^2 = 0} = \frac{p_f \cdot p_i}{k \cdot p_f \; k \cdot p_i} , \quad (13)$$

where p_i (p_f) is the momentum p' or p depending on whether the real photon insertion was on the p' or p leg in the nth order matrix element $\mathcal{M}_{n+1}$ (or its conjugate $\mathcal{M}_{n+1}^\dagger$). Again, the insertion of a $\widetilde{K}$ real photon into an nth order graph leads to a cross section that is proportional to the lower order one, with the cancellation again occurring pair-

8

wise, to give

$$\left|\mathcal{M}_{n+1}^{\widetilde{K}\gamma,\text{tot}}\right|^2 \propto -e^2 \left[\tilde{b}_k(p,p) - 2\tilde{b}_k(p',p) + \tilde{b}_k(p',p')\right] ,$$

$$\equiv -e^2 \widetilde{J}^2(k) . \tag{14}$$

The contributions from the virtual K (Eq. 8) and real $\widetilde{K}$ (Eq. 14) photon corrections are IR divergent and cancel order by order in the theory. We are therefore left with the IR-finite G photon contribution, that we will now evaluate in Sections 5 and 6. However, first, for completeness, we present the LO results.

4 The dark matter annihilation cross section at LO

The leading order (LO) contribution to the annihilation process $\chi\overline{\chi} \to f\overline{f}$ arises from the t- and u-channel processes shown in Fig. 2. The momenta in the CM frame are $q', q \to p', p$, with the choices

$$q'^\mu = (H, 0, 0, P) , \qquad\qquad q^\mu = (H, 0, 0, -P) ,$$
$$p'^\mu = (H, P'\sin\theta, 0, P'\cos\theta) , \qquad p^\mu = (H, -P'\sin\theta, 0, -P'\cos\theta) , \tag{15}$$

where the centre of momentum energy, $s = 4H^2$, and θ is the angle between the initial and final momenta $(\vec{q}', \vec{p}')$. The cross section at leading order for this $2 \to 2$ process is given as usual by,

$$\sigma_{LO} = \frac{1}{64\pi^2 s} \frac{|\vec{p'}|}{|\vec{q'}|} \int d\Omega \left[\sum_{spins} |\mathcal{M}_{LO}^t - \mathcal{M}_{LO}^u|^2\right] ,$$

$$= \frac{1}{32\pi s} \frac{P'}{P} \int d\cos\theta \left[\sum_{spins} |\mathcal{M}_{LO}^t - \mathcal{M}_{LO}^u|^2\right] , \tag{16}$$

where the integration over the azimuth ϕ is trivial, and a summation over both final state and initial state spins is to be performed since all helicity configurations contribute to the total cross section.

The contribution from the matrix element can be expressed as

$$\int d\cos\theta \sum_{spins} |\mathcal{M}_{LO}^t - \mathcal{M}_{LO}^u|^2 \equiv Int_{LO}^t + Int_{LO}^u - Int_{LO}^{tu} ,$$

$$\equiv Int_{LO} , \tag{17}$$

where the subscript LO denotes the LO contribution and the three terms on the right hand side refer to the square of the t-channel matrix element, the square of the u-channel matrix element, and the tu cross terms respectively. Note that the cross term vanishes for Dirac-type dark matter particles. The t-, u-channel matrix elements at LO are given by,

$$\mathcal{M}_{LO}^t = i\lambda^2 \left(\overline{v}(q, m_\chi) P_L v(p, m_f)\right) \Delta(l) \left(\overline{u}(p', m_f) P_R u(q', m_\chi)\right) ,$$
$$\mathcal{M}_{LO}^u = i\lambda^2 \left(\overline{v}(q', m_\chi) P_L v(p, m_f)\right) \Delta(l') \left(\overline{u}(p', m_f) P_R u(q, m_\chi)\right) , \tag{18}$$

9

where we have lightened the notation for the scalar propagator so that $\Delta(l) = i/(l^2 - m_\phi^2)$, and similarly for l', with $l = q - p \equiv p' - q'$ and $l' = q' - p \equiv p' - q$ referring to the momentum of the intermediate scalar for the t and u channels respectively, and $P_{R,L} \equiv (1 \pm \gamma_5)/2$. Adding all the contributions, we find,

$$Int_{LO} = \frac{2\lambda^4}{P\,P'(2H^2 - m_\Phi^2)} \left\{ - \left[H^2 \left(m_\chi^2 - 2m_\Phi^2 \right) + m_\chi^2 P'^2 + m_\Phi^4 \right] \log \frac{\left(2H^2 - m_\Phi^2 + 2P\,P'\right)}{\left(2H^2 - m_\Phi^2 - 2P\,P'\right)} \right.$$
$$\left. + \frac{4P\,P' \left(2H^2 - m_\Phi^2\right) \left(2H^4 - 2H^2 m_\Phi^2 + m_\Phi^4 - 2P^2 P'^2\right)}{4H^4 - 4H^2 m_\Phi^2 + m_\Phi^4 - 4P^2\,P'^2} \right\} \,, \tag{19}$$

where $m_\Phi^2 \equiv m_\chi^2 + m_f^2 - m_\phi^2$. The logarithmic terms arise when either of p, p' are collinear with one of q, q'; however, these are not divergent; they contribute at a single phase space point and are well-behaved. Then the invariant cross section at LO can be written as

$$\sigma_{LO}(s) = \frac{1}{32\pi s} \frac{P'}{P} Int_{LO} \,, \tag{20}$$

where $P'^2 = H^2 - m_f^2$, $P^2 = H^2 - m_\chi^2$, and $4H^2 = s$, the usual Mandelstam variable.

LO cross section in the non-relativistic limit : In the non-relativistic limit, when the velocity of the dark matter particles is small, we can write $P = m_\chi v$ and $H^2 \approx m_\chi^2(1 + v^2)$. Since $P \ll H, m_\Phi$, we can expand the log term as

$$\log \frac{\left(2H^2 - m_\Phi^2 + 2P\,P'\right)}{2H^2 - m_\Phi^2 - 2P\,P'} \xrightarrow{P\ small} 2 \left[\frac{2PP'}{2H^2 - m_\Phi^2} + \frac{2}{3} \left(\frac{2PP'}{2H^2 - m_\Phi^2} \right)^3 + \cdots \right] \,, \tag{21}$$

to get

$$Int_{LO} \xrightarrow{v\ small} \frac{8\lambda^4 m_\chi^2 m_f^2}{(m_\chi^2 + m_\phi^2 - m_f^2)^2} + \mathcal{O}(v^2) \,, \tag{22}$$

Notice that the cross section is proportional to the square of the fermion mass, which is a well-known result [39]. Hence, the LO cross section can be written as

$$\sigma_{LO}(s) = \frac{1}{32\pi s} \frac{P'}{P} Int_{LO} \,,$$
$$\xrightarrow{v\ small} \frac{\lambda^4}{4\pi s} \frac{P'}{P} \left[\frac{m_\chi^2 m_f^2}{(m_\chi^2 + m_\phi^2 - m_f^2)^2} + \mathcal{O}(v^2) \right] \,. \tag{23}$$

This term is the usual velocity-independent "a" term in $s\,\sigma(s)v_{rel} = a + bv^2$ for the annihilation process [39]; with the relative velocity between the two dark matter particles given by $v_{rel} = 2v$, where v is the CM velocity of either of the particles. Terms of order $\mathcal{O}(v^2)$ can be calculated by retaining higher orders in the expansion of Eq. 19.

We can repeat the calculation in the limit when the scalar is much heavier than the other particles, *viz.*, $m_\phi^2 \gg m_\chi^2 \gtrsim m_f^2$. Then $l^2 \equiv (q - p)^2 \ll m_\phi^2$ (where we have implicitly assumed that $\sqrt{s} \ll m_\phi$) and the scalar propagator can be approximated by

$iD_\phi = i/(l^2 - m_\phi^2) \to -i/m_\phi^2$, so that we get

$$Int_{LO}^{\text{heavy scalar}} = \frac{8\lambda^4}{3m_\phi^4} \left[6H^4 - 3H^2 m_\chi^2 + P'^2(2P^2 - 3m_\chi^2) \right] ,$$

$$= \frac{8\lambda^4}{3m_\phi^4} \left[8H^2(H^2 - m_\chi^2) + m_f^2(5m_\chi^2 - 2H^2) \right] , \tag{24}$$

where we have substituted for P, P' in the last line. This gives us a cross section,

$$\sigma_{LO}^{\text{heavy scalar}} = \frac{1}{12\pi s} \frac{P'}{P} \frac{\lambda^4}{m_\phi^4} \left[8H^2(H^2 - m_\chi^2) + m_f^2(5m_\chi^2 - 2H^2) \right] . \tag{25}$$

The first term in the square brackets is proportional to $H^2 = m_\chi^2 \equiv P^2$ and the second is proportional to m_f^2. In the non-relativistic limit, with $H^2 = m_\chi^2(1 + v^2)$, $P = m_\chi v$, this matches the expression given in Eq. 23, with the further approximation, $(m_\chi^2 + m_\phi^2 - m_f^2) \to m_\phi^2$, which is valid in the heavy scalar limit. The important features are instantly visible within this approximation: the $1/m_\phi^4$ dependence arising from the scalar propagator, and the m_f^2 dependence of the cross section in the non-relativistic limit, $H \to m_\chi$. Therefore, we present the NLO calculation of the cross section in the next sections in two parts: in the next section, we present the results in the heavy-scalar limit, where the expressions are shorter and the features can be easily understood. In the subsequent section, we then present the results with the fully dynamical scalar propagator. While the detailed results are cumbersome and can be found on-line [46], the results in the non-relativistic limit have been presented for comparison and discussion here.

5   The dark matter annihilation cross section at NLO—"heavy-scalar" approximation

We apply the Grammer and Yennie technique [42], generalised for the case of thermal field theories as explained in Section 3. There are two sets of contributions at higher order: insertions of a virtual photon in the LO diagrams shown in Fig. 2, as well as insertions of real photons which can be both emitted into or absorbed from the heat bath at temperature T. Each of these contributions can be factorised into K and G (or $\widetilde{K}$ and $\widetilde{G}$) parts for virtual (or real) photon insertions respectively, by applying the Grammer and Yennie technique. As a consequence, the IR divergences are contained in the K ($\widetilde{K}$) contributions respectively and furthermore, were shown earlier to cancel not only at NLO [39], but at all orders [40] in perturbation theory. Note that only soft photon emissions/absorptions of the process $\chi\chi \to f\bar{f}(\gamma)$ are contained in the $\widetilde{K}$ contribution. The hard real-photon emissions/absorptions that contribute to $\widetilde{G}$ photon insertions do not contribute to the process of interest here. Hence, by applying the Grammer and Yennie technique, the NLO corrections to $\chi\chi \to f\bar{f}$ can simply be calculated by computing the G terms of the virtual photon contributions alone.

The various contributions[2] at NLO are shown in Fig. 4. In order to compute the G photon contribution, we will replce the photon propagator by its G photon part; see Eq. 2. Furthermore, throughout this section, we will approximate the scalar propagator by $iD_\phi = i/(l^2 - m_\phi^2) \to -i/m_\phi^2$, and lift this approximation in the next section.

---

[2]Note that fermion self-energy corrections do not contribute to the G photon terms.
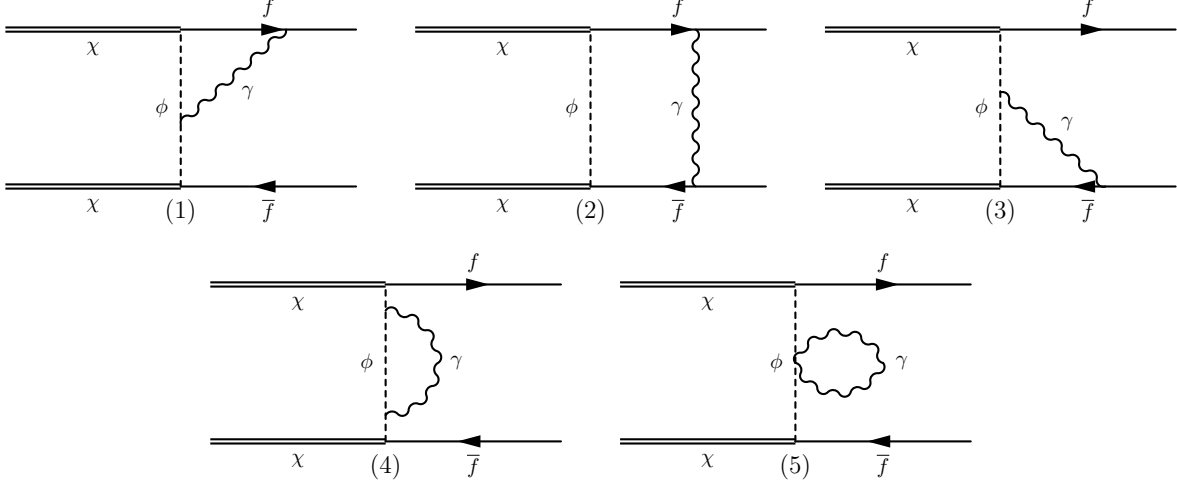
Figure 4: *The t-channel virtual photon corrections to the dark matter annihilation process at next to leading order (NLO). Diagrams are labelled from 1–5. Analogous contributions from the u-channel diagrams exist.*

Analogous to the LO cross section, we can write the next-to-leading order (NLO) virtual contribution as

$$\sigma_{NLO} \quad \propto \quad \left[\sum_{spins} \left(\mathcal{M}^t_{LO} - \mathcal{M}^u_{LO} \right)^\dagger \left(\mathcal{M}^t_{NLO} - \mathcal{M}^u_{NLO} \right) + h.c. \right] , \qquad (26)$$

where each of the higher order t-channel terms in Eq. 26 gets contributions from the five t-channel diagrams shown in Fig. 4 (and similarly, their u-channel counterparts).

We will discuss the details of the calculation using Diagram 1 as an example, before we list the contributions from all the remaining diagrams.

5.1 The NLO contribution from Diagram 1

We start by discussing the pure t-channel NLO contribution from the first diagram in Fig. 4. Since the scalar is very heavy, the thermal contribution from the scalar propagators, which contain a factor $n_\phi = 1/(\exp[\beta E_\phi] - 1)$, can be dropped since $E_\phi \gtrsim m_\phi \gg m_\chi$ and $\beta m_\chi \equiv x \sim 20$ near freeze-out. Hence the scalar propagators can only be of (11) or (22) type; see Appendix A for details on the thermal and temperature independent parts of various propagators. Since all external lines can only be of type-1 [54], and scalar propagators of (12) or (21) type can be neglected, it can be seen that *all* propagators are of type (11) and all vertices are of type-1 alone. In fact, we will find that this holds for all the contributions at NLO, for all the diagrams.

Therefore, there are three possibilities for Diagram 1, *viz.*,

1. the photon propagator (with momentum k) is thermal,

2. the fermion propagator (with momentum $p' + k$) is thermal,

3. or both are thermal,

where, by thermal, we refer to the explicitly T-dependent second term in the propagators as defined in Appendix A. Since the thermal part of all propagators puts the particle on

mass-shell, the last option yields a term depending on the product $\delta(k^2)\,\delta((p'+k)^2-m_f^2)$. Since the external fermion is on-shell, $p'^2 = m_f^2$; hence this product of delta functions requires $p' \cdot k = 0$. But $\delta(k^2)$ implies $k^0 = \pm|\vec{k}|$ or the angle between k and p' should satisfy $\cos\theta_{kp'} = \pm p'^0/|\vec{p'}|$ or $|\cos\theta_{kp'}| > 1$, which is impossible, so there is no phase space available in the case that both propagators are on-shell. Hence we only need to consider the contribution of the first diagram when either one of the photon or the fermion propagator is thermal. In particular, as discussed in Section 3, we only need to consider the IR-finite G-photon contribution with the $g^{\mu\nu}$ term in the photon propagator being replaced by $G^{\mu\nu}$:

$$
\begin{aligned}
-ig^{\mu\nu} &\to -i\left[g^{\mu\nu} - b_k(p_f, p_i)\,k^\mu k^\nu\right] \ , \\
&\equiv -i\left[G_k^{\mu\nu}(p_f, p_i)\right] \ .
\end{aligned} \tag{27}
$$

Since the virtual photon vertices in Diagram 1, Fig. 4 are on the final fermion leg and the scalar, we have $p_f = p'$, $p_i = p$, with $b_k(p_f, p_i)$ defined in Eq. 3. We consider in turn, the contribution from the **thermal** parts of the photon and fermion propagators respectively to the cross section for the process shown in Diagram 1 of Fig. 4. We present the purely t-channel contribution in detail in order to highlight some technicalities, and then go on to the other contributions.

5.1.1 NLO thermal photon contribution to Diagram 1

The matrix element at NLO from the (t-channel) Diagram 1 in Fig. 4 when the G-photon propagator is **thermal**, is given by,

$$
\begin{aligned}
\mathcal{M}_{NLO}^t(\text{Diagram}\,1, \gamma) = &-\int \frac{\mathrm{d}^4k}{(2\pi)^4} \frac{ie^2\lambda^2}{2k\cdot p'}\left(2\pi\delta(k^2)n_B(|k^0|)\right)\Delta(l)\Delta(l+k) \\
&\left[\left(\overline{u}(p', m_f)\gamma_\mu\left(\slashed{k} + \slashed{p}' + m_f\right)P_R\,u(q', m_\chi)\right) \right. \\
&\left. \qquad (k - 2p + 2q)_\nu\,(\overline{v}(q, m_\chi)P_L\,v(p, m_f))\right]\,G_k^{\mu\nu}(p', p) \ , \\
\equiv &\int \frac{\mathrm{d}^4k}{(2\pi)^4}\left(2\pi\delta(k^2)n_B(|k^0|)\right)F_{NLO}^{t,1\gamma}(k) \ ,
\end{aligned} \tag{28}
$$

where n_B is the Bose distribution function given in Eq. A.5 and we have used the index (Diagram $1, \gamma$) to indicate that this is the contribution from Diagram 1 of Fig. 4 when the photon is **thermal**. At this point, we are in a position to justify the simplification of the scalar propagator in the heavy-scalar approximation. The scalar propagator for the t-channel diagrams contains either the inverse of $(l^2 - m_\phi^2)$, or $((l+k)^2 - m_\phi^2)$, with $l \equiv q - p \equiv p' - q'$. Since $m_\chi \ll m_\phi$, $l^2 < m_\phi^2$. Since the photon propagator is **thermal**, $k^2 = 0$ and $l \cdot k \propto |k^0|$ is small since a large $k^0 = |\vec{k}|$ will suppress the contribution due to the presence of the $n_B(|k^0|)$ term. Hence either of the scalar propagators can be approximated by just the $(m_\phi^2)^{-1}$ terms.

A similar reasoning will hold in the next Section 5.1.2 when we consider the fermion propagator to be **thermal**. Then we can write $(l+k)^2 = ((p'+k) - q')^2 \equiv (t - q')^2$ (see Eq. 37). Now $(p'+k)^2 \equiv t^2 = m_f^2$ since the fermion propagator is **thermal** and $t \cdot q$ should be small, otherwise the contribution will be killed by the $n_F(|t^0|)$ term; see Eq. A.4. A similar argument holds for Diagrams 2 and 3 in Fig. 4 when the anti-fermion is thermal, where we can write $(l+k)^2 = (q - p + k)^2 \equiv (q - t)^2$. For the u-channel matrix elements, the scalar momentum is $l' = q' - p$ and the same reasoning applies. Hence we will replace $\Delta(l) = i/(l^2 - m_\phi^2) \to i/(-m_\phi^2)$, etc., in this section. When the scalar is heavy, but not much larger than the dark matter particle or the scale of

the interaction ($\sqrt{s}$), we will reinstate these terms and recompute the cross section in Section 6.

The integration over the photon momentum k can be partly completed using the delta function:

$$
\begin{aligned}
\int \mathrm{d}^4 k \left(2\pi \delta(k^2) \right) F(k) &= 2\pi \int_{-\infty}^{\infty} \mathrm{d}k^0 \int_0^{\infty} K^2 \mathrm{d}K \int \mathrm{d}\Omega_k \left[\delta((k^0)^2 - K^2) \right] F(k^0, K, \Omega_k) , \\
&= 2\pi \int \mathrm{d}k^0 \int \mathrm{d}\Omega_k \int K^2 \mathrm{d}K \frac{\left[\delta(k^0 - K) + \delta(k^0 + K) \right]}{|2k^0|} F(k^0, K, \Omega_k) , \\
&= \pi \int \mathrm{d}\Omega_k \left[\int_0^{\infty} |k^0| \mathrm{d}k^0 F(k^0, k^0, \Omega_k) + \int_{-\infty}^0 |k^0| \mathrm{d}k^0 F(k^0, -k^0, \Omega_k) \right] , \\
&\equiv \pi \int_0^{\infty} \omega \mathrm{d}\omega \left[\int \mathrm{d}\Omega_k F_+(\omega, \omega, \Omega_k) + \int \mathrm{d}\Omega_k F_-(-\omega, \omega, \Omega_k) \right] ,
\end{aligned}
\tag{29}
$$

where $K \equiv |\vec{k}|$. Hence there are two contributions to $\mathcal{M}_{NLO}^t(\text{Diagram } 1, \gamma)$ (and to each such matrix element), one where $K \to k^0 \equiv \omega$, and the other where $K \to -k^0 \equiv -\omega$, as can be seen from Eq. 29. Note that the lower limit ($\omega \to 0$) can be safely taken precisely because the G photon contribution is guaranteed to be IR-finite. The purely t-channel thermal photon contribution from Diagram 1 is therefore given according to Eq. 26 as

$$
\begin{aligned}
\sigma_{NLO}^t(\text{Diagram } 1, \gamma) &= \frac{1}{32\pi s (2\pi)^4} \frac{|\vec{p'}|}{|\vec{q'}|} \int \mathrm{d}\cos\theta \left[\sum_{spins} \left(\mathcal{M}_{LO}^t \right)^\dagger \mathcal{M}_{NLO}^{t,1\gamma} + h.c. \right] , \\
&= \frac{1}{32 s (2\pi)^4} \frac{|\vec{p'}|}{|\vec{q'}|} \int \omega \mathrm{d}\omega\, n_B(\omega) \left[\int \mathrm{d}\cos\theta \int \mathrm{d}\Omega_k \left[F_+^{t,1,\gamma} + F_-^{t,1,\gamma} \right] \right] , \\
&\equiv \frac{1}{32 s (2\pi)^4} \frac{|\vec{p'}|}{|\vec{q'}|} \int \omega \mathrm{d}\omega\, n_B(\omega) Int_{\text{Diagram } 1, \gamma}^t .
\end{aligned}
\tag{30}
$$

On performing the angular integrations, the contribution of this term to the NLO cross section is given by,

$$
Int_{\text{Diagram } 1, \gamma}^t = \frac{64\pi e^2 \lambda^4}{3 m_\phi{}^6 P'} \left(4P' \left(3H^4 + P^2\, P'^2 \right) + \log \frac{H - P'}{H + P'} 3H \left(H^2 + P^2 \right) \left(H^2 + P'^2 \right) \right) .
\tag{31}
$$

Note that the result in Eq. 31 is independent of ω; in fact, the individual F_+ and F_- contributions to $Int_{\text{Diagram } 1, \gamma}^t$ contain some apparent divergent terms of the order of $1/\omega$. When the two terms are added, these cancel, leaving behind IR finite terms that are integrable in ω. This is a reflection of the fact that the G photon insertion was tailored precisely to yield such an IR-finite result. The logarithmic terms arise when p' or p are collinear with q' or q. These will drop out of the final calculation[3]

Similarly, the u-channel and crossed tu-channel NLO contributions from Diagram 1 of Fig. 4 when the photon propagator is thermal can be calculated from the correspond-

---

[3]The collinear terms cancel between the G and $\widetilde{G}$ contributions from the virtual and real corrections respectively [39].

ing u-channel NLO matrix element which is given by

$$\mathcal{M}^u_{NLO}(\text{Diagram}\,1,\gamma) = -\int\frac{\mathrm{d}^4k}{(2\pi)^4}\frac{ie^2\lambda^2}{2k\cdot p'}\left(2\pi\delta(k^2)n_B(|k^0|)\right)\Delta(l')\Delta(l'+k)$$
$$\left[\left(\overline{u}(p',m_f)\gamma_\mu\left(\slashed{k}+\slashed{p}'+m_f\right)P_R\,u(q,m_\chi)\right)\left(k-2p+2q'\right)_\nu\right.$$
$$\left.\left(\overline{v}(q',m_\chi)P_L\,v(p,m_f)\right)\right]G_k^{\mu\nu}(p',p)\,. \tag{32}$$

Then the total NLO contribution from (the t-, u and cross tu channels of) Diagram 1, Fig. 4, with thermal photon propagator is given by,

$$Int^{tt+uu-tu}_{\text{Diagram}\,1,\gamma} = \frac{64\pi e^2\lambda^4}{3m_\phi^6 P'}\left[24H^4P' - 6H^2m_\chi^2P' - 6m_\chi^2P'\left(m_f^2+3P'^2\right) + 8P^2P'^3\right.$$
$$\left.+\log\frac{H-P'}{H+P'}\left(6H^5 + H^3\left(6\left(P^2+P'^2\right)-3m_\chi^2\right)+3HP'^2\left(2P^2-3m_\chi^2\right)\right)\right]\,,$$
$$= \frac{64\pi e^2\lambda^4}{3m_\phi^6 P'}\left[4P'\left(8H^4 - 2\,H^2\left(4m_\chi^2+m_f^2\right)+5m_\chi^2m_f^2\right)\right.$$
$$\left.+3\log\frac{H-P'}{H+P'}\left(8H^5 - 4H^3\left(2m_\chi^2+m_f^2\right)+5Hm_\chi^2m_f^2\right)\right]\,,$$
$$\xrightarrow{\text{non-coll}}\frac{256\pi e^2\lambda^4}{3m_\phi^6}\left(8H^4 - 2\,H^2\left(4m_\chi^2+m_f^2\right)+5m_\chi^2m_f^2\right)\,, \tag{33}$$

where we have substituted for $P'^2 = H^2 - m_f^2$, $P^2 = H^2 - m_\chi^2$ and dropped the collinear logarithmic terms in the last line. It can be seen that $Int^{tt+uu-tu}_{\text{Diagram}\,1,\gamma}$ given in Eq. 33 is independent of ω; hence the final contribution from thermal photons to Diagram 1, Fig. 4 is

$$\sigma^{tt+uu-tu}_{NLO}(\text{Diagram}\,1,\gamma) = \frac{1}{32s(2\pi)^4}\,\frac{P'}{P}\int\omega\mathrm{d}\omega\,n_B(\omega)Int^{tt+uu-tu}_{\text{Diagram}\,1,\gamma}\,,$$
$$= \frac{1}{32s(2\pi)^4}\,\frac{P'}{P}\,\frac{\pi^2T^2}{6}\times Int^{tt+uu-tu}_{\text{Diagram}\,1,\gamma}\,, \tag{34}$$

where the T^2 temperature dependence of the cross section arises due to the ω-independence of $Int^{tt+uu-tu}_{\text{Diagram}\,1,\gamma}$, with

$$\int_0^\infty\omega\mathrm{d}\omega\,n_B(\omega) = \frac{\pi^2T^2}{6}\,. \tag{35}$$

We now discuss the contribution at NLO from Diagram 1, Fig. 4, when the fermion propagator is thermal.

5.1.2 NLO thermal fermion contribution to Diagram 1

As mentioned earlier, the thermal contributions from Diagram 1 only arise when either the photon or fermion propagator is thermal, that is, the explicitly T-dependent second term of the propagators in Eqs. A.2 and A.3 contribute; the contribution when both are thermal vanishes. We now consider the contribution at NLO of the t-channel Diagram 1, Fig. 4, when the photon propagator is non-thermal, but the fermion propagator is thermal. Recall that only the photon contributions give rise to IR divergences (both at $T=0$ and finite temperature). This is because of their differing thermal distributions;

see Eqs. A.5 and A.4. In addition, we have shown in Section 3.1.2 that the K-photon contribution when the photon is inserted into a **thermal** fermion vanishes; see Eq. 11. Hence in the G photon insertion, which arises from $G^{\mu\nu} = (g^{\mu\nu} - b_k k^\mu k^\nu)$, the second term, which is the K photon piece, vanishes and we therefore need consider just the $g^{\mu\nu}$ contribution (or in other words, since the K contribution vanishes, the G term contains the entire $g^{\mu\nu}$ contribution). The corresponding matrix element is then given by

$$
\mathcal{M}^t_{NLO}(\text{Diagram}\,1, f) = -\int \frac{\mathrm{d}^4 k}{(2\pi)^4} \frac{ie^2\lambda^2}{k^2} \frac{g^{\mu\nu}}{k^2} \left(-2\pi\delta((p'+k)^2 - m_f^2) n_F(|(p'+k)^0|)\right)
$$
$$
\Delta(l)\Delta(l+k) \left[\left(\overline{u}(p', m_f)\gamma_\mu \left(\slashed{k} + \slashed{p}' + m_f\right) P_R\, u(q', m_\chi)\right)\right.
$$
$$
\left. \left(k + 2p' - 2q'\right)_\nu \left(\overline{v}(q, m_\chi) P_L\, v(p, m_f)\right)\right] , \tag{36}
$$

where n_F is the fermion number operator defined in Eq. A.4, the $1/k^2$ term arises from the **temperature-independent** part of the photon propagator, and the delta-function from the **thermal** fermion propagator. As before, the index $(\text{Diagram}\,1, f)$ refers to the contribution arising from Diagram 1, Fig. 4, when the **thermal** part of the fermion propagator contributes. The sign difference between n_F and n_B is what dictates the IR finite nature of the fermionic contributions. It is convenient to define $p' + k \equiv t$, and change the variable of integration to t, so that

$$
\mathcal{M}^t_{NLO}(\text{Diagram}\,1, f) = \int \frac{\mathrm{d}^4 t}{(2\pi)^4} \frac{ie^2\lambda^2}{2} \frac{g^{\mu\nu}}{m_f^2 - t\cdot p'} \left(2\pi\delta(t^2 - m_f^2) n_F(|t^0|)\right)
$$
$$
\Delta(l)\Delta(l+k) \left[\left(\overline{u}(p', m_f)\gamma_\mu \left(\slashed{t} + m_f\right) P_R\, u(q', m_\chi)\right)\right.
$$
$$
\left. \left(t + p' - 2q'\right)_\nu \left(\overline{v}(q, m_\chi) P_L\, v(p, m_f)\right)\right] , \tag{37}
$$

so that the same simplification can be done using the delta-function as discussed in Eq. 29, to obtain

$$
\int \mathrm{d}^4 t \left[2\pi\delta(t^2 - m_f^2)\right] F(t) = 2\pi \int \mathrm{d}^4 t\, \delta(t_0^2 - |\vec{t}|^2 - m_f^2) F(t) \equiv 2\pi \int \mathrm{d}^4 t\, \delta(t_0^2 - \omega_t^2) F(t) ,
$$
$$
= \pi \int_{m_f}^\infty K_t\, \mathrm{d}\omega_t \left[\int \mathrm{d}\Omega_t F_+(\omega_t, \omega_t, \Omega_t) + \int \mathrm{d}\Omega_t F_-(-\omega_t, \omega_t, \Omega_t)\right] , \tag{38}
$$

where $\omega_t^2 = |\vec{t}|^2 + m_f^2 \equiv K_t^2 + m_f^2$ and we have expressions for $F_\pm(t)$ analogous to that in Eq. 29. Then the **thermal** fermion contribution to the purely t-channel Diagram 1 is given analogously to that for **thermal** photons in Eq. 30 by

$$
\sigma^t_{NLO}(\text{Diagram}\,1, f) = \frac{1}{32\pi s (2\pi)^4} \frac{|\vec{p'}|}{|\vec{q'}|} \int \mathrm{d}\cos\theta \left[\sum_{spins} \left(\mathcal{M}^t_{LO}\right)^\dagger \mathcal{M}^{t,1f}_{NLO} + h.c.\right] ,
$$
$$
= \frac{1}{32 s (2\pi)^4} \frac{|\vec{p'}|}{|\vec{q'}|} \int K_t \mathrm{d}\omega_t\, n_F(\omega_t) \left[\int \mathrm{d}\cos\theta \int \mathrm{d}\Omega_t \left[F_+^{t,1,f} + F_-^{t,1,f}\right]\right] ,
$$
$$
\equiv \frac{1}{32 s (2\pi)^4} \frac{|\vec{p'}|}{|\vec{q'}|} \int K_t \mathrm{d}\omega_t\, n_F(\omega_t) Int^t_{\text{Diagram}\,1, f} . \tag{39}
$$

Again, on completing the angular integration, we find the t-channel thermal fermion contribution to Diagram 1, Fig. 4, to be

$$
\begin{aligned}
Int^t_{\text{Diagram}\,1,f} = \frac{32\pi e^2\lambda^4}{3K_t m_\phi^6 P'} \Big[&4K_t P'\left(3H^2 m_\chi^2 + P^2\left(4H^2 - m_f^2\right)\right) \\
&- \left(6H^5\omega_t - 3H^4 m_f^2 + H^3\omega_t\left(4P^2 - 3m_f^2\right) - 4H^2 m_f^2 P^2 - H\omega_t P^2\left(m_f^2 - 2P'^2\right)\right. \\
&\left.- m_f^2 P^2(P'^2 - m_f^2)\right)\log\frac{H\omega_t + K_t P' - m_f^2}{H\omega_t - K_t P' - m_f^2} \\
&+ \left(6H^5\omega_t + 3H^4 m_f^2 + H^3\omega_t\left(4P^2 - 3m_f^2\right) + 4H^2 m_f^2 P^2 - H\omega_t P^2\left(m_f^2 - 2P'^2\right)\right. \\
&\left.+ m_f^2 P^2\left(P'^2 - m_f^2\right)\right)\log\frac{H\omega_t - K_t P' + m_f^2}{H\omega_t + K_t P' + m_f^2}\Big] .
\end{aligned}
\tag{40}
$$

While the non-logarithmic terms are (as in the case of thermal photons) independent of ω_t, the logarithmic terms have a complicated dependence on ω_t through K_t and it is not possible to analytically integrate these terms. A simplification is achieved in the limit that the fermion masses can be neglected in comparison to ω_t, so that $K_t \to \omega_t$. Then the contribution simplifies[4] to

$$
Int^t_{\text{Diagram}\,1,f} \xrightarrow{K_t \to \omega_t} \frac{64\pi e^2 H\lambda^4}{3m_\phi^6 P'}\Big[2HP'\left(3m_\chi{}^2 + 4P^2\right) \\
- 2\left(3H^4 + 2H^2 P^2 + P^2 P'^2\right)\log\frac{H + P'}{H - P'}\Big] ,
\tag{41}
$$

with

$$
\frac{\log[H\omega_t + K_t P' \pm m_f^2]}{\log[H\omega_t - K_t P' \pm m_f^2]} \xrightarrow{K_t \to \omega_t} \frac{\log[H + P']}{\log[H - P']} ,
\tag{42}
$$

where we have dropped terms of order $\mathcal{O}(m_f^2/(H\omega_t))$, so that these logarithmic terms are of the same form as before, independent of ω_t, yielding again a T^2 temperature dependence from this contribution, using[5]

$$
\int_{m_f}^{\infty} K_t \mathrm{d}\omega_t\, n_F(\omega_t) \approx \int_0^{\infty} \omega_t \mathrm{d}\omega_t\, n_F(\omega_t) = \frac{\pi^2 T^2}{12} .
\tag{43}
$$

Similarly, the u-channel matrix element for thermal fermions is given by:

$$
\begin{aligned}
\mathcal{M}^u_{NLO}(\text{Diagram}\,1, f) = -\int \frac{\mathrm{d}^4 t}{(2\pi)^4}\frac{ie^2\lambda^2\, g^{\mu\nu}}{2(m_f^2 - t\cdot p')}&\left(-2\pi\delta(t^2 - m_f^2)n_F(|t^0|)\right) \\
\Delta(l')\Delta(l' + k)\big[&\left(\overline{u}(p', m_f)\gamma_\mu\left(\slashed{t} + m_f\right)P_R\, u(q, m_\chi)\right) \\
&\left(t + p' - 2q\right)_\nu\left(\overline{v}(q', m_\chi)P_L\, v(p, m_f)\right)\big] .
\end{aligned}
\tag{44}
$$

Using the LO matrix elements given in Eq. 18, the NLO matrix element for the t-channel contribution given in Eqs. 36 and 37 and that for the u-channel contribution in Eq. 44, the total thermal fermion contribution from Diagram 1, Fig. 4, that is, from

---

[4]Note that no approximations have been made in the non-logarithmic term.

[5]Expanding $K_t = \sqrt{\omega_t^2 - m_f^2}$ as $K_t \approx \omega_t - m_f^2/(2\omega_t) + \cdots$ is not a possible choice since $\int (\mathrm{d}\omega_t/\omega_t)n_F$ is not convergent; it is of course possible to integrate this numerically if more precise results are required.

the combined t-channel, u-channel, and the crossed tu-channel, is found to be

$$
Int^{tt+uu-tu}_{\text{Diagram}\,1,f} = \frac{32\pi e^2 \lambda^4}{3m_\phi^6 K_t P'} \Big[4K_t P' \left(3m_\chi^2 m_f^2 + 2P^2(4H^2 - m_f^2)\right)
$$

$$
+ 3m_\chi^2 \log \frac{H\omega_t + K_t P' - m_f^2}{H\omega_t - K_t P' - m_f^2} \left(3H^3\omega_t - 2H^2 m_f^2 + H\omega_t(P'^2 - 2m_f^2) + m_f^4 - P'^2 m_f^2\right)
$$

$$
- 3m_\chi^2 \log \frac{H\omega_t + K_t P' + m_f^2}{H\omega_t - K_t P' + m_f^2} \left(3H^3\omega_t + 2H^2 m_f^2 + H\omega_t(P'^2 - 2m_f^2) - m_f^4 + P'^2 m_f^2\right)
$$

$$
- 2 \log \frac{H\omega_t + K_t P' - m_f^2}{H\omega_t - K_t P' - m_f^2} \left(6H^5\omega_t - 3H^4 m_f^2 + H^3\omega_t(4P^2 - 3m_f^2) - 4H^2 P^2 m_f^2\right.
$$

$$
\left. - H\omega_t P^2(m_f^2 - 2P'^2) - P^2 m_f^2(P'^2 - m_f^2)\right)
$$

$$
- 2 \log \frac{H\omega_t + K_t P' + m_f^2}{H\omega_t - K_t P' + m_f^2} \left(6H^5\omega_t + 3H^4 m_f^2 + H^3\omega_t(4P^2 - 3m_f^2) + 4H^2 P^2 m_f^2\right.
$$

$$
\left. - H\omega_t P^2(m_f^2 - 2P'^2) + P^2 m_f^2(P'^2 - m_f^2)\right) \Big] \ . \quad (45)
$$

As in the case of the t-channel contribution alone, we can again use the approximation given in Eq. 42, so that

$$
Int^{tt+uu-tu}_{\text{Diagram}\,1,f} \xrightarrow{K_t \to \omega_t} \frac{128\pi e^2 \lambda^4}{3m_\phi^6} \left[\left(3m_\chi^2 m_f^2 + 2P^2(4H^2 - m_f^2)\right) - \frac{3H}{2P'} \log \frac{H + P'}{H - P'} \left\{ 4H^4 + \right.\right.
$$

$$
\left.\left. 2H^2\left(8P^2 - 2m_\chi^2 - m_f^2\right) + m_f^2\left(3m_\chi^2 - 2P^2\right)\right\} \right] \ .
$$

$$
(46)
$$

Again $Int^{1,tt+uu-tu,f}_{NLO}$ is independent of ω_t; hence, the ω_t integral (see Eq. 43) gives a T^2 temperature dependence to the cross section (analogue of Eq. 39 for all channels) from the thermal fermions in Diagram 1, Fig. 4, as well.

5.2 Total thermal contribution to the NLO cross section

Now that we have demonstrated details of the calculation of the cross section from Diagram 1, Fig. 4, we present the detailed results from all Diagrams in Fig. 4. Diagram 3 is similar to Diagram 1; here also, it is clear from an analysis similar to that for Diagram 1 in Section 5.1 that only one of the photon and fermion propagators can be thermal at a time. Note that Diagrams 4 and 5 have no fermion propagators while Diagram 2 has three propagators (excluding that of the scalar) and can in principle have contributions from any one, any two, or all three propagators being thermal (where we remind the reader that by thermal we mean the contribution from the explicitly T-dependent second term in the expressions for the photon and fermion propagators given in Eqs. A.2 and A.3). As argued for Diagrams 1 and 3, there is no consistent available kinematic phase space when the photon propagator and either one of the fermion or anti-fermion propagators are both thermal. Hence there is no contribution from the case when all three propagators in Diagram 2 are thermal (all three propagators contribute on-shell) as well as when the photon propagator and either the fermion or anti-fermion propagator is thermal. Left is the case when the fermion and anti-fermion propagators are thermal, but not the photon one. Here, we find that the delta function constraint $\delta((p' + k)^2 - m_f^2)\delta((p - k)^2 - m_f^2)$ is satisfied for the single phase space point, $k^0 = 0$.

Therefore, for all the diagrams, as long as we discard the negligible contribution from scalar thermal propagators, we only have thermal contributions when exactly one of the propagators in the diagram is thermal and the others contribute through their non-thermal or temperature-independent parts.

We now go on to present the contributions from the remaining Diagrams 2–5 in Fig. 4 as well as their u-channel counterparts. As can be observed from the diagrams in Fig. 4 itself, Diagrams 1, 3 and 5 have two scalar propagators, Diagram 4 has three, and Diagram 2 as well as the LO matrix element have one scalar propagator each. Hence it is expected that the contributions of Diagram 4 will be suppressed compared to the other contributions. As before, we have only one propagator whose thermal part contributes, and we separately list the contributions from the terms when the photon propagator is thermal and when the fermion/anti-fermion one is thermal. We begin with the thermal photon contributions.

5.2.1   Total thermal photon contributions to the cross section

The NLO matrix elements for the remaining Diagrams 2–5, Fig. 4, when the thermal part of the photon propagator is taken into account are analogous to the expression given in Eq. 30 and are given in Appendix B. The corresponding contributions from Diagrams 2–5 to the cross section (corresponding to Eqs. 30, 33, 34 from Diagram 1) from both the t- and u-channels and crossed tu-channel (in the heavy scalar propagator limit) are given by,

$$Int^{tt+uu-tu}_{\text{Diagram}\,2,\gamma} = \frac{64\pi e^2 \lambda^4}{3m_\phi^4} \left[\left(6H^2 - 6m_\chi^2 + 2P^2\right) + \frac{1}{HP'}\log\frac{H-P'}{H+P'}\left(3H^2 - P^2\right)\,\left(H^2 - P'^2\right) \right] \,,$$

$$(47)$$

$$Int^{tt+uu-tu}_{\text{Diagram}\,3,\gamma} = \frac{64\pi e^2 \lambda^4}{3m_\phi^6 P'} \left[2P'\left(6H^4 + H^2\left(8P^2 - 3m_\chi^2\right) + \left(3m_\chi^2 - 2P^2\right)\left(m_f^2 - P'^2\right)\right) \right.$$
$$+ H\log\frac{H-P'}{H+P'}\left(12H^4 + H^2\left(-9m_\chi^2 - 6m_f^2 + 8P^2\right)\right.$$
$$\left.\left. + m_\chi^2\left(6m_f^2 - 3P'^2\right) - 2P^2\left(m_f^2 - 2P'^2\right)\right) \right] \,,$$

$$(48)$$

$$Int^{tt+uu-tu}_{\text{Diagram}\,4,\gamma} = \frac{512\pi e^2 \lambda^4}{15m_\phi^8 P'(H^2 - P'^2)} \left[P'\left\{60H^8 - 30H^6\left(2m_\chi^2 - m_f^2 + 2P'^2\right)\right.\right.$$
$$+ 15H^4\left(m_\chi^4 - m_\chi^2\left(m_f^2 - 2P'^2\right) + 2P^2\left(3m_f^2 + 2P'^2\right)\right)$$
$$- H^2\left[5m_\chi^2\left(m_f^2\left(P^2 + 3P'^2\right) + 2P'^2\left(P^2 - 3P'^2\right)\right)\right.$$
$$\left. + 2P^2\left(m_f^2\left(15P'^2 - 4P^2\right) + 30P'^4\right)\right]$$
$$\left. - P'^2\left(15m_\chi^4 P'^2 + 5m_\chi^2 P^2\left(m_f^2 - 2P'^2\right) + 2m_f^2 P^4\right)\right\}$$
$$+ \log\frac{H-P'}{H+P'}Hm_f^2\left(H^2 - P'^2\right)\left\{30H^4 - 5H^2\left(3m_\chi^2 - 8P^2\right)\right.$$
$$\left.\left. - 15m_\chi^2 P'^2 + 4P^4 + 10P^2 P'^2\right\}\right] \,,$$

$$(49)$$

$$Int^{tt+uu-tu}_{\text{Diagram}\,5,\gamma} = \frac{512\pi e^2 \lambda^4}{3m_\phi^6}\left(-6H^4 + 3H^2 m_\chi^2 + P'^2\left(3m_\chi^2 - 2P^2\right)\right) \,.$$

$$(50)$$

Simplifying, and substituting $P'^2 \to H^2 - m_f^2$ and $P^2 \to H^2 - m_\chi^2$, and dropping the collinear terms, the total contribution from all terms where the virtual photon propagator is thermal, is given by

$$Int_{Total,\gamma T}^{tt+uu-tu} = \left\{ \left[Int_{\text{Diagram 2},\gamma}^{tt+uu-tu} \right] + \left[Int_{\text{Diagram 1},\gamma}^{tt+uu-tu} + Int_{\text{Diagram 3},\gamma}^{tt+uu-tu} + Int_{\text{Diagram 5},\gamma}^{tt+uu-tu} \right] + \left[Int_{\text{Diagram 4},\gamma}^{tt+uu-tu} \right] \right\} ,$$

$$= \frac{128\pi e^2 \lambda^4}{3} \left\{ \frac{1}{m_\phi^4} \left[4P^2 \right] - \frac{2}{m_\phi^6} H^2 \left[H^2 - m_\chi^2 - P^2 \right] + \frac{4}{5m_\phi^8} \left[90H^6 - 120H^4(m_\chi^2 - P^2) \right. \right.$$

$$+ H^2 (30m_\chi^4 + 5m_\chi^2(9m_f^2 - 4P^2) - 6P^2(5m_f^2 - P^2))$$

$$\left. \left. + m_f^2(-15m_\chi^4 + 15m_\chi^2 P^2 + 2P^4) \right] \right\} ,$$

$$= \frac{512\pi e^2 \lambda^4}{15} \left\{ \frac{5}{m_\phi^4} \left(H^2 - m_\chi^2 \right) + \frac{H^2}{m_\phi^8} \left[216H^4 - 272H^2 m_\chi^2 + 56m_\chi^4 \right] \right.$$

$$\left. - \frac{m_f^2}{m_\phi^8} \left[28H^4 - 86H^2 m_\chi^2 + 28m_\chi^4 \right] \right\} , \tag{51}$$

where we have combined contributions having the same number of scalar propagators. A few points can be noted. From the first line, we see that the total thermal photon contribution from Diagrams 1, 3, and 5 vanishes, since $P^2 = H^2 - m_\chi^2$. Hence terms contributing as $1/m_\phi^6$ from thermal photon insertions vanish. Also, from the last line in Eq. 51, we see that the contribution from Diagram 2 (contributing as $1/m_\phi^4$) is proportional to $H^2 - m_\chi^2 = P^2$ and is small in the non-relativistic limit. So also is the contribution from Diagram 4 $(1/m_\phi^8)$ term since the term proportional to H^2 also vanishes when $H = m_\chi$ (exact non-relativistic limit), leaving only the m_f^2 dependent term. The familiar independence on ω is seen for the total thermal photon contribution at NLO, so that the total cross section from these terms again has a T^2 temperature dependence. We now calculate the contribution from thermal fermions.

5.2.2 Total thermal fermion contributions to the cross section

Only Diagrams 1–3 in Fig. 4 contribute to the NLO cross section when the thermal part of the fermion propagator is considered. The corresponding matrix elements for Diagrams 2 and 3 are also given in Appendix B. The contributions to the NLO cross section from each of these diagrams (in the heavy scalar limit, where we have substituted for P' and dropped the logarithmic terms, which have the same form as for Diagram 1), are given by

$$Int_{\text{Diagram 2},f}^{tt+uu-tu} = -\frac{32\pi e^2 \lambda^4}{3m_\phi^4 \left(H^2 - \omega_t^2 \right)} \left(12H^2(H^2 - m_\chi^2) + 4H^2 P^2 + 2\omega_t^2(3(H^2 - m_\chi^2) + P^2) \right) ,$$

$$Int_{\text{Diagram 2},\bar{f}}^{tt+uu-tu} = Int_{\text{Diagram 2},f}^{tt+uu-tu} ,$$

$$Int_{\text{Diagram 3},\bar{f}}^{tt+uu-tu} = \frac{128\pi e^2 \lambda^4}{3m_\phi^6} \left(3m_\chi^2 m_f^2 + 2P^2(4H^2 - m_f^2) \right) . \tag{52}$$

20

Notice that the contribution of the thermal fermion from Diagram 3 is the same as that from Diagram 1, as can be seen[6] from Eq. 46. Furthermore, the contribution of the thermal fermion from Diagram 2, Fig. 4 has non-trivial ω_t dependences both in the numerator and denominator. Recognising that large values of ω_t will lead to vanishing of the corresponding distribution function, $n_F(|\omega_t|)$, we expand the denominator for $\omega_t < H$ (recall that $H \geq m_\chi$ and $\beta m_\chi = x \sim 20$ at freeze-out) to obtain the total thermal fermion contribution from Diagram 2 to be

$$Int^{tt+uu-tu}_{\text{Diagram}\,2,f+\overline{f}} = -\frac{64\pi e^2 \lambda^4}{3m_\phi^4 H^2}\left(12H^2(H^2 - m_\chi^2) + 4H^2P^2 + 6\omega_t^2(3(H^2 - m_\chi^2) + P^2)\right)\,.$$

(53)

The presence of the ω_t^2 terms in the numerator will lead to T^4 temperature dependence in the cross section[7]. Then, the total contribution from all terms where the virtual fermion (or anti-fermion) propagator is thermal, is given by

$$\begin{aligned}
Int^{tt+uu-tu}_{Total,(f+\overline{f})T} &= \left[Int^{tt+uu-tu}_{\text{Diagram}\,1,f} + Int^{tt+uu-tu}_{\text{Diagram}\,3,\overline{f}}\right] + \left[Int^{tt+uu-tu}_{\text{Diagram}\,2,f} + Int^{tt+uu-tu}_{\text{Diagram}\,2,\overline{f}}\right]\,,\\
&= \frac{64\pi e^2 \lambda^4}{3m_\phi^6}\left\{\left[12m_\chi^2 m_f^2 + 8P^2(4H^2 - m_f^2)\right] - m_\phi^2\left[12(H^2 - m_\chi^2) + 4P^2\right.\right.\\
&\quad \left.\left. + \frac{6\omega_t^2}{H^2}\left(3(H^2 - m_\chi^2) + P^2\right)\right]\right\}\,.
\end{aligned}$$

(54)

The total invariant NLO cross section is then given by the sum of the thermal photon and thermal fermion contributions,

$$\begin{aligned}
\sigma_{NLO}(s) &= \frac{1}{32s(2\pi)^4}\frac{P'}{P}\left[\int \omega\,d\omega\,n_B Int^{tt+uu-tu}_{Total,\gamma T} + \int K_t d\omega_t\,n_F Int^{tt+uu-tu}_{Total,(f+\overline{f})T}\right]\,,\\
&= \frac{\lambda^4}{12\pi s}\frac{P'}{P}\left[\frac{8\alpha T^2}{15}\right] \times \left\{\frac{1}{m_\phi^4}\left[\frac{7\pi^2 T^2}{4H^2}(H^2 - m_\chi^2)\right] + \frac{1}{m_\phi^6}\left[5m_\chi^2 m_f^2 + 2P^2(4H^2 - m_f^2)\right]\right.\\
&\quad \left. + \frac{1}{m_\phi^8}\left[8H^2(27H^4 - 34H^2 m_\chi^2 + 7m_\chi^4) - 2m_f^2(14H^4 - 43H^2 m_\chi^2 + 14m_\chi^4)\right]\right\}\,;
\end{aligned}$$

(55)

here $s = 4H^2$ and the terms have been ordered in increasing powers of m_ϕ^2 in the denominator. We have replaced K_t by ω_t in the integrand of the second term in order to obtain an analytical result and furthermore, presented the results, taking the lower limit of the integration to be zero. Notice that the leading term $(1/m_\phi^4)$ is of order $\mathcal{O}(T^4)$ and is further suppressed by $(H^2 - m_\chi^2) = P^2$ in the non-relativistic limit. The terms suppressed by an additional propagator factor $(\sim 1/m_\phi^6)$ contribute at T^2 order and are either proportional to m_f^2 $(\sim 5m_\chi^2 m_f^2)$ or to P^2, which is small is the non-relativistic limit. However, these terms, of order $\mathcal{O}(H^2 P^2 T^2/m_\phi^6)$ or $\mathcal{O}(m_\chi^2 m_f^2 T^2/m_\phi^6)$, can have significant contribution in the relativistic regime when P is large.

The NLO cross section in the non-relativistic limit : Freeze-out occurs around $m_\chi/T \sim 20$ so that the dark matter particles can be considered to be non-relativistic at this point, with $P \to m_\chi v$, and $H^2 \to m_\chi^2(1 + v^2)$, so that Eqs. 51 and

---

[6]Note the absence of odd powers of ω_t due to the symmetry explicit in Eq. 8.

[7]Since $H^2 - m_\chi^2 = p^2$, both the ω_t^0 and the ω_t^2 terms are small in the non-relativistic limit.

54 reduce to

$$Int_{Total,\gamma T}^{tt+uu-tu} \overset{v \; small}{\longrightarrow} \frac{512\pi e^2 \lambda^4}{15 m_\phi{}^8} \left\{ 30 m_\chi^4 m_f^2 (1+v^2) + 5 m_\phi^4 m_\chi^2 v^2 \right\} \;,$$

$$Int_{Total,(f+\bar{f})T}^{tt+uu-tu} \overset{v \; small}{\longrightarrow} \frac{64\pi e^2 \lambda^4}{3 m_\phi^6} \left\{ \left[6 m_\chi^2 m_f^2 + 4 m_\chi^2 v^2 (4 m_\chi^2 - m_f^2) \right] + 8 m_\phi^2 m_\chi^2 v^2 \left(3 \frac{\omega_t^2}{H^2} - 2 \right) \right\} \;.$$
(56)

It can be seen that the NLO cross section (obtained from Eqs. 55 and 56) is proportional to m_f^2 as $v \to 0$, just as the LO cross section; see Eq. 22. This can be understood from helicity conservation: just as in the LO case, the NLO diagrams (with an additional virtual photon) that we have computed are planar $2 \to 2$ processes. The Majorana coupling then forces the final states into the "wrong" chirality so that the cross section is proportional to the fermion mass squared. At early times in the evolution of the Universe, the dark matter particles are relativistic, $\sqrt{s}$ can be large, and there is less suppression in the annihilation into the lighter fermions. This also holds for freeze-in scenarios where $m_\chi/T \sim \mathcal{O}(1)$. Now that we have understood the structure of the NLO contributions in the heavy-scalar limit, we will go on to include the entire scalar propagator in the calculation of the NLO cross section.

6 The dark matter annihilation cross section at NLO including the "dynamical" scalar propagator

We repeat the calculation of the previous section without making the heavy scalar assumption, $i.e.$, retaining the "dynamical" scalar propagator, $iD_\phi = i/(l^2 - m_\phi^2)$, where $l = q - p$ is the momentum of the scalar. As we had already argued in Section 5.1.1, $l \cdot k, k^2 \ll m_\phi^2$; hence, we expand the relevant propagator terms, for instance,

$$\frac{1}{(l+k)^2 - m_\phi^2} = \frac{1}{(l^2 - m_\phi^2) + (2l \cdot k + k^2)}$$
$$\approx \frac{1}{(l^2 - m_\phi^2)} \left[1 - \frac{(2l \cdot k + k^2)}{(l^2 - m_\phi^2)} \right] \;.$$
(57)

Similar expansions can be obtained for the u-channel scalar propagators as well. This enables us to get analytic expressions for the NLO cross section. However, the results are rather cumbersome and opaque; they are available as Mathematica [50] Notebooks in Ref. [46]. We simply make a few remarks on the calculation and specifically on the non-relativistic limit which is of interest at freeze-out.

The main difference on including the momentum dependence of the scalar is the increase in complexity of the $\cos\theta$ angular integration due to the presence of the term $l^2 - m_\phi^2 \equiv m_\chi^2 + m_f^2 - m_\phi^2 - 2q \cdot p \equiv m_\Phi^2 - 2(H^2 - PP'\cos\theta)$ in the denominator. It will be seen that this gives rise to logarithms of the type $\log\left(2H^2 - m_\Phi^2 \pm 2P\,P'\right)$ which we have already encountered when calculating the LO cross section.

Once again, the leading $\mathcal{O}(T^2)$ terms are ω- (ω_t)-independent for the thermal photon

(fermion) cases, while the ω^2 (ω_t^2) terms contribute to the $\mathcal{O}(T^4)$ terms. We have,

$$\sigma_{NLO}(s) = \frac{1}{32s(2\pi)^4}\frac{P'}{P}\left[\int \mathrm{d}\omega\omega\, n_B\, Int_{Total,\gamma T}^{tt+uu-tu} + \int \mathrm{d}\omega_t\omega_t\, n_F\, Int_{Total,(f+\bar{f})T}^{tt+uu-tu}\right] ,$$

$$\xrightarrow{v\ small} \frac{\lambda^4}{4\pi s}\frac{P'}{P}\frac{\pi\alpha T^2}{6}\left[Int_{NLO}^a + v^2\, Int_{NLO}^b\right] , \tag{58}$$

where the expression in the second line refers to the so-called a and b terms that contribute in the non-relativistic limit.

It is interesting to note that the pattern is the same as with the heavy scalar computation in the previous section. The leading behaviour from naive counting of the scalar propagator is expected to have the form (from Diagram 2)

$$\sigma_{NLO}(s) \propto \frac{m_\chi^2 T^2}{(2H^2 - m_\Phi^2 + 2PP')(2H^2 - m_\Phi^2 - 2PP')} , \tag{59}$$

where the denominator (proportional to m_ϕ^4 in the heavy scalar limit) is the analogous term to the $1/m_\phi^4$ contribution in the heavy-scalar limit. However, as in the previous section with heavy-scalar assumption, we find this term vanishes and the leading contribution is again

$$\sigma_{NLO}(s) \propto \frac{m_\phi^2 M^2 m_f^2 T^2}{(4H^4 - 4m_\Phi^2 H^2 + m_\Phi^4 - 4P^2 P'^2)^2} ,$$

$$\propto \frac{M^2 m_f^2 T^2}{m_\phi^6} , \tag{60}$$

where M^2 is any combination of $H \equiv \sqrt{s}/2, m_\chi$ or m_f, of dimension 2.

As mentioned earlier, the results for the general relativistic case are available as sets of Mathematica Notebooks at the web-page Ref. [46]. Here we will discuss some aspects of the results in the non-relativistic limit, which are of relevance near freeze-out, when $m_\chi/T \sim 20$.

NLO cross section in the non-relativistic limit :

In the limit when $p \to m_\chi v$, and the expressions are expanded for small velocities, the cross section can be expressed as $\sigma v = a + bv^2$. The contributions to the "a" term from all the diagrams (see Eq. 58 for the definition) are listed in Table 1. Both $\mathcal{O}(T^2)$ and $\mathcal{O}(T^4)$ terms contribute. (The $\mathcal{O}(v^2)$ terms can be found from the expressions given online in Ref. [46].) In the non-relativistic limit, the denominator in the full expressions reduces to the form visible in Table 1:

$$\frac{1}{(4H^4 - 4H^2 m_\Phi^2 + m_\Phi^4 - 4P^2 P'^2)^n} \approx \frac{1}{(m_\chi^2 - m_f^2 + m_\phi^2)^n}\left[1 - \frac{4nP^2 m_\phi^2}{(m_\chi^2 - m_f^2 + m_\phi^2)}\right] ,$$

$$\xrightarrow{v\to 0} \frac{1}{(m_\chi^2 - m_f^2 + m_\phi^2)^n} \equiv \frac{1}{D^n} , \tag{61}$$

as was encountered in the LO expression for the cross section in Eq. 23. It can be seen from Table 1 that, in the non-relativistic limit, the "a" terms in the cross section are proportional to the square of the fermion mass, both at order $\mathcal{O}(T^2)$ and $\mathcal{O}(T^4)$, just as in the LO case. Again, as with the NLO calculation in the heavy-scalar limit, the potential leading contribution at order $1/m_\phi^4$ is suppressed by a factor of P^2 and

contributes[8] at the order $\mathcal{O}(P^2 T^4 m_\phi^6/(m_\chi^2 D^5)) \sim \mathcal{O}(P^2 T^4/(m_\chi^2 m_\phi^4))$, as before. Hence, the leading contribution is again at order $\mathcal{O}(1/m_\phi^6)$, as mentioned earlier. Note that only Diagrams 2 and 4 have $\mathcal{O}(T^4)$ contributions; that from Diagram 4 is highly suppressed due to the $1/D^5 \sim 1/m_\phi^{10}$ denominator factor. In general, it can be seen that the leading contributions are of order $\mathcal{O}(m_f^2 m_\chi^2 T^2/m_\phi^6)$ in the non-relativistic limit.

Diagram	γ/f	Int_{NLO}^a (T^2 contribution)	Int_{NLO}^a (T^4 contribution)
1	γ	$-8m_\chi^2 m_f^2(m_f^2 - m_\phi^2)/D^4$	0
	f	$4m_\chi^2 m_f^2(5m_\chi^2 - 5m_f^2 + m_\phi^2)/D^4$	0
	$\text{Total}_{\gamma+f}$	$2m_\chi^2 m_f^2(5m_\chi^2 - 9m_f^2 + 5m_\phi^2)/D^4$	0
2	γ	$-8m_\chi^2 m_f^2/D^3$	0
	f	$-6m_f^2(2m_\chi^2 - m_f^2)/D^3$	$-\frac{21\pi^2 T^2}{10 m_\chi^2 D^3}m_f^2(2m_\chi^2 - m_f^2)$
	$\text{Total}_{\gamma+f}$	$-m_f^2(14m_\chi^2 - 3m_f^2)/D^3$	$-\frac{21\pi^2 T^2}{10 m_\chi^2 D^3}m_f^2(2m_\chi^2 - m_f^2)$
3	γ	$-8m_\chi^2 m_f^2(m_f^2 - m_\phi^2)/D^4$	0
	f	$4m_\chi^2 m_f^2(3m_\chi^2 - 2m_f^2 + m_\phi^2)/D^4$	0
	$\text{Total}_{\gamma+f}$	$2m_\chi^2 m_f^2(3m_\chi^2 - 6m_f^2 + 5m_\phi^2)/D^4$	0
4	γ	$32m_\chi^4 m_f^2/D^4$	$-\frac{56\pi^2 T^2}{15 D^5}m_\chi^2 m_f^2(m_\chi^2 - m_f^2)$
5	γ	$-16m_\chi^2 m_f^2/D^3$	0
All	$\text{Total}_{\gamma+f}$	$\frac{1}{D^3}m_f^2(2m_\chi^2 + 3m_f^2) +$ $\frac{2}{D^4}m_f^2 m_\chi^2(10m_\phi^2 + 24m_\chi^2 - 15m_f^2)$	$-\frac{21\pi^2 T^2}{10 m_\chi^2 D^3}m_f^2(2m_\chi^2 - m_f^2) +$ $-\frac{56\pi^2 T^2}{15 D^5}m_\chi^2 m_f^2(m_\chi^2 - m_f^2)$

Table 1: *The $v \to 0$ contributions from various diagrams to the NLO cross section (the so-called "a" terms in the non-relativistic cross section); see Eqs. 58 and 61 for definitions. The second column lists the $\mathcal{O}(T^2)$ contributions while the third one lists the $\mathcal{O}(T^4)$ contributions; note that an overall factor of T^2 has been removed from the terms. Here D is defined as $D = (m_\chi^2 - m_f^2 + m_\phi^2)$.*

Considering only the corresponding "a" (v^0) terms in the non-relativistic limit, the

---

[8]Expressions for the "b" term in the cross section are given online in Ref. [46]; note that these are not necessarily proportional to m_f^2.

relative size of the NLO contribution *for each* flavour of fermion pair is given by,

$$\frac{\sigma_{NLO}^a}{\sigma_{LO}^a} = \frac{\pi \alpha T^2}{6 m_\phi^2} \frac{m_f^2 (22 m_\chi^2 + 3 m_f^2)}{m_f^2 m_\chi^2} \ ,$$

$$\approx \frac{11 \pi \alpha}{3} \frac{T^2}{m_\phi^2} \ , \tag{62}$$

where we have used $D \sim m_\phi^2$ and dropped terms in σ_a^{NLO} having higher powers of $D = m_\phi^2$ in the denominator.

7 Discussions and Conclusion

We have computed the next-to-leading order thermal contributions to the cross section for dark matter annihilation into fermion pairs. We have used a Lagrangian which couples the dark matter Majorana fermions to standard model fermions via charged scalar doublets. We use the real time formulation of thermal field theory to compute the higher order contributions to the cross section for the annihilation of dark matter particles[9] via $\chi\chi \to f\bar{f}$ in a heat bath of fermions, scalars and photons at temperature T. Note that the regime of interest is during the evolution of the Universe when electroweak symmetry breaking is complete so that we consider higher order corrections only from photons, since the W and Z are by now massive. We assume in addition that the scalars are heavy, $m_\phi \gtrsim m_\chi$.

We have used the generalised Grammer and Yennie [42–44] technique where the cancellation of infra-red soft divergences is straightforward. This is achieved by separating the photon propagator into the sum of K and G parts. This can be realised in the thermal case as well, where the propagators are now sums of temperature-independent and temperature-dependent 2×2 matrices; we label the latter as the thermal part of the propagator since it carries an explicit temperature dependence. It was shown earlier [40, 41] that the infrared (IR) divergences (which are much more acute than at zero temperature, being linear rather than logarithmically divergent in the soft limit) are completely contained in the K photon contribution and the G photon term is finite. The infrared divergences cancel against similar terms from real soft photon contributions; note that both absorption from, and emission into the heat bath is required to be included for these cancellations to occur.

While the use of the Grammer and Yennie technique (and its modification for thermal field theories) is well-known for demonstration of the cancellations of IR divergences in various contexts, it has been rarely used, so far as the authors are aware, to actually compute the IR-finite remainder. In the present work, we have computed the NLO finite G photon contributions to the dark matter annihilation cross section using this technique and found its application to be straightforward. A further simplification occurred since kinematically it turns out that the total contribution to the NLO cross section is actually a sum of terms where *any one* of the (photon, fermion, anti-fermion) propagators can be thermal at a time. Hence the Grammer and Yennie approach allows a great simplification of the problem and consequent ease of computation.

The calculation was first done by replacing the full scalar propagator $1/(l^2 - m_\phi^2)$ by just the mass term, $1/(-m_\phi^2)$, valid when the scalar is very heavy. This enabled

---

[9]Since the dark matter particles are taken to be Majorana fermions, the annihilation occurs via the t-, u- and cross tu-channel processes; Dirac dark matter particles will have the same interaction where the tu cross terms vanish.

us to have simpler expressions so that the pattern of dependence of the NLO cross section on both the temperature T as well as the energy scales, $H = \sqrt{s}/2$ and m_f, was visible. The five diagrams that contribute at NLO are shown in Fig. 4 for the t-channel processes with analogous diagrams for the u-channel ones.

The potential leading contribution[10] at order $1/m_\phi^4$ in the scalar mass (from Diagram 2) is of order $\mathcal{O}(p^2 T^4/(H^2 m_\phi^4))$, which is small in the non-relativistic limit when p^2 is small. Hence the leading contribution is at order $1/m_\phi^6$. It was found that the $\mathcal{O}(T^2)$ contribution to the NLO cross section at this order is proportional to either $(m_f^2 M^2 T^2/m_\phi^6)$ or to $(p^2 M^2 T^2/m_\phi^6)$ where $M^2 \sim H^2$ or m_χ^2. Hence in the non-relativistic regime (at around $m_\chi/T \sim 20$) where freeze-out occurs, the momentum-dependent term can be ignored and the NLO cross section is proportional to the square of the fermion mass; this dependence is also seen in the LO cross section and occurs due to the Majorana nature of the dark matter particles and consequent helicity suppression. It is likely that the NLO terms retain this feature due to the $2 \to 2$ planar nature of the contributing diagrams.

The calculation was repeated, retaining the full dynamical scalar propagator. The essential features of the calculation remain the same. Since the expressions are very long, we present here only the leading "a" term of the cross section in the non-relativistic limit (contribution to σv when $v \to 0$) in Table 1; the entire solution in the relativistic case as well as their non-relativistic approximations are listed in the Mathematica Notebooks available online [46]. We find that both the $\mathcal{O}(T^2)$ and the $\mathcal{O}(T^4)$ contributions to the "a" term are proportional to m_f^2, as can be seen from Table 1. As with the heavy-scalar approximation, the potential leading contribution at order $1/m_\phi^4$ is suppressed by a factor of p^2 and contributes at the order $\mathcal{O}(p^2 T^4 m_\phi^6/(m_\chi^2 D^5))$ which reduces, in the limit $m_\phi > m_\chi$, to the order $\mathcal{O}(p^2 T^4/(m_\chi^2 m_\phi^4))$, as before. Hence, the leading contribution is again at order $1/m_\phi^6$, leading to a relative NLO thermal contribution which is $\sim 10\,(\alpha T^2/m_\phi^2)$ times the LO cross section.

In summary, the NLO thermal correction terms have a T^2 dependence, but are suppressed by additional powers of the (heavy scalar) propagator as well as by the square of the fermion masses. This was discussed in Ref. [39] where the NLO thermal cross section was initially computed to be of order $\mathcal{O}(T^2)$, and later it was shown that the T^2 contributions vanish and the leading contribution is in fact of order $\mathcal{O}(T^4)$. This result was strengthened in Ref. [45] where an operator product expansion (OPE) approach was used to show the same result (for Dirac-type dark matter particles); here, the scalar propagator was again reduced to just the mass term $(1/(-m_\phi^2))$, and it was argued that $\mathcal{O}(m_f^2 T^2/m_\chi^4)$ are small compared to $\mathcal{O}(T^4/m_\chi^4)$ and were thus ignored.

In this work, we have retained the fermion masses and found that, in the non-relativistic limit, the leading terms as $v \to 0$ at both order $\mathcal{O}(T^2)$ and $\mathcal{O}(T^4)$ are suppressed by m_f^2, just as the LO cross section. The general results when T may be large, so $x = m_\chi/T \sim \mathcal{O}(1)$, are given without making the non-relativistic approximation, in Mathematica notebooks [46]. These corrections may be significant in a freeze-in scenario in the early Universe when T is larger for light dark matter candidates where $m_\chi/T \gtrsim 1$.

Thermal corrections to such cross sections can become important in the early Universe where the thermally averaged cross section, $\langle \sigma v \rangle$, appears as the collision term in the Boltzmann equation for the evolution of the dark matter phase space densities, or

---

[10]This is the order at which the LO cross section contributes; see Eqs. 19, 20 and 23.

equivalently, their yields. We have

$$\langle \sigma \cdot v_{\text{Møl}} \rangle \equiv \frac{\int \sigma \cdot v_{\text{Møl}} \exp[-E_1/T] \exp[-E_2/T] \mathrm{d}^3 p_1 \mathrm{d}^3 p_2}{\int \exp[-E_1/T] \exp[-E_2/T] \mathrm{d}^3 p_1 \mathrm{d}^3 p_2} \ . \tag{63}$$

Here p_1, p_2 are the momenta of the annihilating dark matter particles, and $v_{\text{Møl}} = \sqrt{(p_1 \cdot p_2)^2 - m_\chi^2}$. The Boltzmann approximation for the dark matter number densities has been used. For cross sections of the form $\sigma v = a + bv^2$, we have

$$\langle \sigma v \rangle = a + \frac{3}{2} bT \ . \tag{64}$$

Hence, the thermal corrections that we have computed at NLO will yield a correction,

$$\langle \sigma_{NLO} v \rangle = \langle (a_1 T^2 + a_2 T^4) + v^2 (b_1 T^2 + b_2 T^4) \rangle \ ,$$
$$= (a_1 T^2 + a_2 T^4) + \frac{3}{2} (b_1 T^3 + b_2 T^5) \ . \tag{65}$$

The corrections from the NLO thermal contribution to "b" (the terms proportional to v^2 and higher powers) can therefore be neglected. These thermal corrections to the cross section $\sigma(s)$ can alter the yield equation and hence the final relic density, especially in freeze-in scenarios. This is acquiring importance [55] in view of the increasingly precise measurements of the relic density [2, 6]. It will be interesting to pursue this further, within the frame-work of the Grammer and Yennie formulation where the calculation is simpler; this is beyond the scope of the present work.

A   Feynman rules in thermal field theory

The scalar propagator is given by

$$iS_{\text{scalar}}^{t_a,t_b}(p,m) = \begin{pmatrix} \Delta(p) & 0 \\ 0 & \Delta^*(p) \end{pmatrix} + 2\pi\delta(p^2 - m^2) n_{\text{B}}(|p^0|) \begin{pmatrix} 1 & e^{|p^0|/(2T)} \\ e^{|p^0|/(2T)} & 1 \end{pmatrix} , \tag{A.1}$$

where $\Delta(p) = i/(p^2 - m^2 + i\epsilon)$, and $t_a, t_b \ (= 1, 2)$ refer to the field's thermal type. We shall refer to the first term as the temperature-independent part and the second as the thermal part in the main text since it carries explicit temperature dependence; note that the latter contributes only on mass-shell. Only the thermal parts can convert type-1 to type-2 fields, and vice versa; type-1 fields are the physical fields.

In the Feynman gauge, the photon propagator corresponding to a momentum k is given by

$$i\mathcal{D}_{\mu\nu}^{t_a,t_b}(k) = -g_{\mu\nu} iD^{t_a,t_b}(k) = -g_{\mu\nu} \, iS_{\text{scalar}}^{t_a,t_b}(k,0) \ , \tag{A.2}$$

and the fermion propagator at zero chemical potential is given by

$$iS_{\text{fermion}}^{t_a,t_b}(p,m) = \begin{pmatrix} S & 0 \\ 0 & S^* \end{pmatrix} - 2\pi S' \delta(p^2 - m^2) n_{\text{F}}(|p^0|) \begin{pmatrix} 1 & \epsilon(p_0) e^{|p^0|/(2T)} \\ -\epsilon(p_0) e^{|p^0|/(2T)} & 1 \end{pmatrix} ,$$
$$\equiv (\not{p} + m) \begin{pmatrix} F_p^{-1} & G_p^{-1} \\ -G_p^{-1} & F_p^{*-1} \end{pmatrix} ,$$
$$\equiv (\not{p} + m) \overline{S}^{t_a,t_b}(p,m) \ , \tag{A.3}$$

where $S = i/(\not{p} - m + i\epsilon)$, and $S' = (\not{p} + m)$; hence the entire fermion propagator is proportional to $(\not{p} + m)$, just as at $T = 0$. It can be seen that all propagators are a sum of temperature-independent and thermal parts. The fermionic number operator,

$$n_\text{F}(|p^0|) \equiv \frac{1}{\exp\{|p^0|/T\} + 1} \xrightarrow{p^0 \to 0} \frac{1}{2} , \tag{A.4}$$

is well-defined in the soft limit; however, the bosonic number operator contributes an additional power of k^0 in the denominator to the photon propagator in the soft limit:

$$n_\text{B}(|k^0|) \equiv \frac{1}{\exp\{|k^0|/T\} - 1} \xrightarrow{k^0 \to 0} \frac{T}{|k^0|} , \tag{A.5}$$

so that the leading IR divergence in the finite temperature part is linear rather than logarithmic as was the case at zero temperature. (The cancellation of IR divergence thus involves cancellation of the leading linear divergence as well as the logarithmic sub-divergence.)

The fermion–photon vertex factor is given by $(-ie\gamma_\mu)(-1)^{t_\mu+1}$, where $t_\mu = 1, 2$ for the type-1 and type-2 vertices. The scalar–photon vertex factor is $[-ie(p_\mu + p'_\mu)](-1)^{t_\mu+1}$ where p_μ (p'_μ) is the 4-momentum of the scalar entering (leaving) the vertex, while the 2-scalar–2-photon *seagull* vertex factor (see Fig. 5) is $[+2ie^2 g_{\mu\nu}](-1)^{t_\mu+1}$ (the factor '2' is dropped for a *tadpole* vertex). At a given vertex, all fields are of the same type.

a. Fermion-Photon Vertex   b. Scalar-Photon Vertex   c. Seagull Vertex
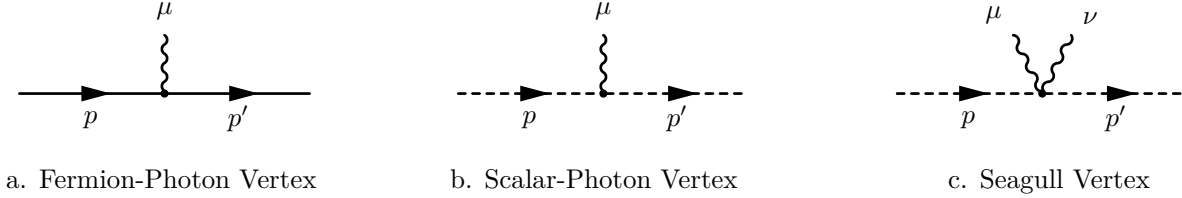
Figure 5: *Allowed vertices for fermion–photon and scalar–photon interactions.*

The bino-scalar-fermion vertex factor is $i\lambda P_L$; for details on Feynman rules for Majorana particles at zero temperature, see Ref. [56]. An overall negative sign applies as usual to the type-2 bino vertex; again all fields at a vertex are of the same type.

A.1   Some identities at finite temperature

Various identities useful for fermions are given in Ref. [40] and are reproduced here for completeness. Note that Eqs. A.1, A.2 and A.3 lead to

$$(\not{p} - m) \, iS_p^{t_a,t_b} = i(-1)^{t_a+1}\delta_{t_a,t_b} , \tag{A.6}$$

where we have used the compressed notation, $iS^{t_a,t_b}(p,m) \equiv iS_p^{t_a,t_b}$.

Consider the insertion of the μ vertex of the additional virtual photon with momentum k between vertices μ_{q+1} and μ_q on the p' fermion leg; see Fig. 3. The momentum of the photon at the vertex μ_q is l_q, with Lorentz index μ_q, and thermal type-index t_q. Hence the momentum of the fermion leg to the left of the vertex μ_q is $p' + \sum_{i=1}^{q} l_i$

which we denote as $p' + \sum_q$. Using Eq. A.6, we have,

$$S_{p'+\sum\limits_q}^{t_q,t_\mu} \slashed{k} \, S_{p'+\sum\limits_q+k}^{t_\mu,t_{q+1}} = (-1)^{t_\mu+1} \left[S_{p'+\sum\limits_q}^{t_q,t_{q+1}} \delta_{t_\mu,t_q+1} - S_{p'+\sum\limits_q+k}^{t_q,t_{q+1}} \delta_{t_\mu,t_q} \right] \ . \tag{A.7}$$

If the photon vertex is inserted to the right of the vertex labelled '1' on the fermion leg with momentum p', we have,

$$\overline{u}(p')\slashed{k}S_{p'+k}^{t_\mu,t_1} = \overline{u}(p')(-1)^{t_\mu+1}\delta_{t_\mu,t_1} \ , \tag{A.8}$$

since $\slashed{p}'u(p') = mu(p')$. Similar relations hold for the insertion of of the virtual K photon at a vertex ν on the (anti-)fermion p leg since $\slashed{p}\,u(p) = m\,u(p)$ as well.

B   Matrix elements for $\chi\chi \to f\overline{f}$ at NLO

As described in the text, the matrix elements are sums of the contributions when any one of the photon, fermion or anti-fermion propagators is thermal, that is, contributes via its explicitly temperature-dependent part. The t- and u- channel matrix elements for Diagram 1 when either the photon or fermion propagator is thermal is given in the text, in Eqs. 28, 32, 36, and 44. The remaining matrix elements are listed below. In the equations that follow, the indices (Diagram i, γ), (Diagram i, f) and (Diagram $i, \overline{f}$) refer to the contribution from Diagram i ($i = 1$–5), when the photon, fermion, or anti-fermion respectively contribute via the explicitly thermal parts of their propagators.

The thermal photon contributions from the last four diagrams in Fig. 4 are given by

$$\mathcal{M}_{NLO}^t(\text{Diagram}\,2, \gamma) = \int \frac{\mathrm{d}^4 k}{(2\pi)^4} \frac{ie^2\lambda^2}{4k\cdot p'k\cdot p} \left(2\pi\delta(k^2)n_B(|k^0|)\right) (i\Delta(l+k))$$
$$\left[\left(\overline{u}(p',m_f)\gamma_\mu \left(\slashed{k}+\slashed{p}'+m_f\right) P_R\,u(q',m_\chi)\right)\right.$$
$$\left.\left(\overline{v}(q,m_\chi)P_L\left(\slashed{k}-\slashed{p}+m_f\right)\gamma_\nu\,v(p,m_f)\right)\right] G_k^{\mu\nu}(p',p) \ ,$$

$$\mathcal{M}_{NLO}^t(\text{Diagram}\,3, \gamma) = \int \frac{\mathrm{d}^4 k}{(2\pi)^4} \frac{ie^2\lambda^2}{2k\cdot p} \left(2\pi\delta(k^2)n_B(|k^0|)\right) \Delta(l)\Delta(l+k)$$
$$\left[\left(\overline{u}(p',m_f)P_R\,u(q',m_\chi)\right)(k-2p+2q)_\mu\right.$$
$$\left.\left(\overline{v}(q,m_\chi)P_L\left(\slashed{k}-\slashed{p}+m_f\right)\gamma_\nu\,v(p,m_f)\right)\right] G_k^{\mu\nu}(p,p) \ ,$$

$$\mathcal{M}_{NLO}^t(\text{Diagram}\,4, \gamma) = \int \frac{\mathrm{d}^4 k}{(2\pi)^4} (ie^2\lambda^2) \left(2\pi\delta(k^2)n_B(|k^0|)\right) \Delta(l)i\Delta(l+k)\Delta(l)$$
$$\left[\left(\overline{u}(p',m_f)P_R\,u(q',m_\chi)\right)(k-2p+2q)_\mu\,(k-2p+2q)_\nu\right.$$
$$\left.\left(\overline{v}(q,m_\chi)P_L\,v(p,m_f)\right)\right] G_k^{\mu\nu}(p,p) \ ,$$

$$\mathcal{M}_{NLO}^t(\text{Diagram}\,5, \gamma) = \int \frac{\mathrm{d}^4 k}{(2\pi)^4} (ie^2\lambda^2) \left(2\pi\delta(k^2)n_B(|k^0|)\right) \Delta(l)\Delta(l)$$
$$\left[\left(\overline{u}(p',m_f)P_R\,u(q',m_\chi)\right)\left(\overline{v}(q,m_\chi)P_L\,v(p,m_f)\right)\right] G_k^{\mu\nu}(p,p) \ , \tag{B.9}$$

for the t-channel, and appropriately crossed ones for the u-channel, for example, as shown in Eq. 32 for the contribution from the first diagram. The matrix elements for the case when the fermion or anti-fermion is thermal arise only from Diagrams 1, 2, and

3. They are given by

$$
\begin{aligned}
\mathcal{M}^t_{NLO}(\text{Diagram}\, 2, f) = \int \frac{\mathrm{d}^4 t}{(2\pi)^4} & \frac{ie^2\lambda^2\, g^{\mu\nu}}{4(m_f^2 - p'\cdot t)\,(p\cdot p' + m_f^2 - t\cdot(p+p'))} \\
& \left(-2\pi\delta(t^2 - m_f^2)n_F(|t^0|)\right) i\Delta(l+k) \left[\left(\overline{u}(p', m_f)\gamma_\mu \left(\slashed{t} + m_f\right)\right.\right. \\
& \left.\left. P_R\, u(q', m_\chi)\right) \left(\overline{v}(q, m_\chi) P_L \left(\slashed{t} - \slashed{p'} - \slashed{p}\right)\gamma_\nu v(p, m_f)\right)\right]\ ,
\end{aligned}
$$

$$(\text{B.10})$$

$$
\begin{aligned}
\mathcal{M}^t_{NLO}(\text{Diagram}\, 2, \overline{f}) = \int \frac{\mathrm{d}^4 t}{(2\pi)^4} & \frac{ie^2\lambda^2\, g^{\mu\nu}}{4(m_f^2 - p\cdot t)\,(p\cdot p' + m_f^2 - t\cdot(p+p'))} \\
& \left(-2\pi\delta(t^2 - m_f^2)n_F(|t^0|)\right) i\Delta(l+k) \left[\left(\overline{u}(p', m_f)\gamma_\mu \left(-\slashed{t} + \slashed{p'} + \slashed{p} + m_f\right)\right.\right. \\
& \left.\left. P_R\, u(q', m_\chi)\right) \left(\overline{v}(q, m_\chi) P_L \left(-\slashed{t} + m_f\right)\gamma_\nu v(p, m_f)\right)\right]\ ,
\end{aligned}
$$

$$(\text{B.11})$$

$$
\begin{aligned}
\mathcal{M}^t_{NLO}(\text{Diagram}\, 3, \overline{f}) = \int \frac{\mathrm{d}^4 t}{(2\pi)^4} & \frac{ie^2\lambda^2\, g^{\mu\nu}}{2(m_f^2 - t\cdot p)} \left(-2\pi\delta(t^2 - m_f^2)n_F(|t^0|)\right) \Delta(l)\Delta(l+k) \\
& \left[\left(\overline{u}(p', m_f)P_R\, u(q', m_\chi)\right) (-t - p + 2q)_\mu\right. \\
& \left. \left(\overline{v}(q, m_\chi) P_L \left(-\slashed{t} + m_f\right) v(p, m_f)\right)\right]\ .
\end{aligned}
$$

$$(\text{B.12})$$

Here f corresponds to the fermion being thermal in Diagram 2 and $\overline{f}$ corresponds to the anti-fermion being thermal in Diagrams 2 and 3 respectively. We use the same replacement technique here as explained in Eqs. 37 and 38 for the thermal fermion contribution to Diagram 1. For the matrix element of Diagram 2, we have substituted $t = p' + k$ as for Diagram 1; and we have substituted $t = p - k$ when the anti-fermion is thermal. Analogous expressions hold for the u-channel matrix elements.

References

[1] R. L. Workman et al. "Review of Particle Physics". In: *PTEP* 2022 (2022), p. 083C01. DOI: 10.1093/ptep/ptac097.

[2] N. Aghanim et al. "Planck 2018 results. VI. Cosmological parameters". In: *Astron. Astrophys.* 641 (2020). [Erratum: Astron.Astrophys. 652, C4 (2021)], A6. DOI: 10.1051/0004-6361/201833910. arXiv: 1807.06209 [astro-ph.CO].

[3] Antonio Circiello et al. *Constraining Dark Matter Annihilation with Fermi-LAT Observations of Ultra-Faint Compact Stellar Systems*. Apr. 2024. arXiv: 2404.01181 [astro-ph.HE].

[4] Pavel E. Mancera Piña et al. *Exploring the nature of dark matter with the extreme galaxy AGC 114905*. Apr. 2024. arXiv: 2404.06537 [astro-ph.GA].

[5] Keith Bechtol et al. "Snowmass2021 Cosmic Frontier White Paper: Dark Matter Physics from Halo Measurements". In: *Snowmass 2021*. Mar. 2022. arXiv: 2203.07354 [hep-ph].

[6] Luca Amendola et al. "Cosmology and fundamental physics with the Euclid satellite". In: *Living Rev. Rel.* 21.1 (2018), p. 2. DOI: 10.1007/s41114-017-0010-3. arXiv: 1606.00180 [astro-ph.CO].

[7] Laura Baudis. "Dark matter searches". In: *Annalen Phys.* 528 (2016), pp. 74–83. DOI: 10.1002/andp.201500114. arXiv: 1509.00869 [astro-ph.CO].

[8] N. Arkani-Hamed, A. Delgado, and G. F. Giudice. "The Well-tempered neutralino". In: *Nucl. Phys. B* 741 (2006), pp. 108–130. DOI: 10.1016/j.nuclphysb.2006.02.010. arXiv: hep-ph/0601041.

[9] Yu-Tong Chen et al. *Light Thermal Dark Matter Beyond p-Wave Annihilation in Minimal Higgs Portal Model*. Mar. 2024. arXiv: 2403.02721 [hep-ph].

[10] Giorgio Arcadi et al. *The Waning of the WIMP: Endgame?* Mar. 2024. arXiv: 2403.15860 [hep-ph].

[11] Elias Bernreuther et al. *Dark matter relic density in strongly interacting dark sectors with light vector mesons*. Nov. 2023. arXiv: 2311.17157 [hep-ph].

[12] Martin Bauer and Tilman Plehn. *Yet Another Introduction to Dark Matter: The Particle Physics Approach*. Vol. 959. Lecture Notes in Physics. Springer, 2019. DOI: 10.1007/978-3-030-16234-4. arXiv: 1705.01987 [hep-ph].

[13] Yann Gouttenoire. *Beyond the Standard Model Cocktail*. Springer Theses. Cham: Springer, 2022. ISBN: 978-3-031-11862-3, 978-3-031-11861-6. DOI: 10.1007/978-3-031-11862-3. arXiv: 2207.01633 [hep-ph].

[14] Leszek Roszkowski, Enrico Maria Sessolo, and Sebastian Trojanowski. "WIMP dark matter candidates and searches—current status and future prospects". In: *Rept. Prog. Phys.* 81.6 (2018), p. 066201. DOI: 10.1088/1361-6633/aab913. arXiv: 1707.06277 [hep-ph].

[15] Gianfranco Bertone and Dan Hooper. "History of dark matter". In: *Rev. Mod. Phys.* 90.4 (2018), p. 045002. DOI: 10.1103/RevModPhys.90.045002. arXiv: 1605.04909 [astro-ph.CO].

[16] Katherine Garrett and Gintaras Duda. "Dark Matter: A Primer". In: *Adv. Astron.* 2011 (2011), p. 968283. DOI: 10.1155/2011/968283. arXiv: 1006.2483 [hep-ph].

[17] Pablo Figueroa, Gonzalo Herrera, and Fredy Ochoa. *Direct detection of light dark matter charged under a $L_\mu - L_\tau$ symmetry*. Apr. 2024. arXiv: 2404.03090 [hep-ph].

[18] Ciaran A. J. O'Hare. *Cosmology of axion dark matter*. Mar. 2024. arXiv: 2403.17697 [hep-ph].

[19] Anirban Das et al. *Energy-dependent Boosted Dark Matter from Diffuse Supernova Neutrino Background*. Mar. 2024. arXiv: 2403.15367 [hep-ph].

[20] Manimala Chakraborti, Sven Heinemeyer, and Ipsita Saha. *Consistent Excesses in the Search for $\tilde{\chi}_2^0 \tilde{\chi}_1^\pm$: Wino/bino vs. Higgsino Dark Matter*. Mar. 2024. arXiv: 2403.14759 [hep-ph].

[21] Xiao-Gang He et al. *Scalar dark matter explanation of the excess in the Belle II $B^+ \to K^+ + invisible$ measurement*. Mar. 2024. arXiv: 2403.12485 [hep-ph].

[22] Shao-Ping Li. *Observable CMB spectrum distortions from dark matter annihilation*. Feb. 2024. arXiv: 2402.16708 [hep-ph].

[23] Pedro De la Torre Luque, Shyam Balaji, and Joseph Silk. *New 511 keV line data provides strongest sub-GeV dark matter constraints*. Dec. 2023. arXiv: 2312.04907 [hep-ph].

[24] Paolo Gondolo and Graciela Gelmini. "Cosmic abundances of stable particles: Improved analysis". In: *Nucl. Phys. B* 360 (1991), pp. 145–179. DOI: 10.1016/0550-3213(91)90438-4.

[25] Stefano Profumo, Leonardo Giani, and Oliver F. Piattella. "An Introduction to Particle Dark Matter". In: *Universe* 5.10 (2019), p. 213. DOI: 10.3390/universe5100213. arXiv: 1910.05610 [hep-ph].

[26] J. Silk et al. *Particle Dark Matter: Observations, Models and Searches*. Ed. by Gianfranco Bertone. Cambridge: Cambridge Univ. Press, 2010. ISBN: 978-1-107-65392-4. DOI: 10.1017/CBO9780511770739.

[27] Stefano Profumo. *An Introduction to Particle Dark Matter*. World Scientific, 2017. ISBN: 978-1-78634-000-9, 978-1-78634-001-6, 978-1-78634-001-6. DOI: 10.1142/q0001.

[28] Nicolás Bernal et al. "The Dawn of FIMP Dark Matter: A Review of Models and Constraints". In: *Int. J. Mod. Phys. A* 32.27 (2017), p. 1730023. DOI: 10.1142/S0217751X1730023X. arXiv: 1706.07442 [hep-ph].

[29] Matthew Baumgart et al. *Snowmass White Paper: Effective Field Theories for Dark Matter Phenomenology*. Mar. 2022. arXiv: 2203.08204 [hep-ph].

[30] Martin Beneke, Robert Szafron, and Kai Urban. "Sommerfeld-corrected relic abundance of wino dark matter with NLO electroweak potentials". In: *JHEP* 02 (2021), p. 020. DOI: 10.1007/JHEP02(2021)020. arXiv: 2009.00640 [hep-ph].

[31] Martin Beneke, Robert Szafron, and Kai Urban. "Wino potential and Sommerfeld effect at NLO". In: *Phys. Lett. B* 800 (2020), p. 135112. DOI: 10.1016/j.physletb.2019.135112. arXiv: 1909.04584 [hep-ph].

[32] Michael Klasen, Florian Lyonnet, and Farinaldo S. Queiroz. "NLO+NLL collider bounds, Dirac fermion and scalar dark matter in the B–L model". In: *Eur. Phys. J. C* 77.5 (2017), p. 348. DOI: 10.1140/epjc/s10052-017-4904-8. arXiv: 1607.06468 [hep-ph].

[33] J. Harz et al. "One-loop corrections to neutralino-stop coannihilation revisited". In: *Phys. Rev. D* 91.3 (2015), p. 034028. DOI: 10.1103/PhysRevD.91.034028. arXiv: 1409.2898 [hep-ph].

[34] M. Laine. "Resonant s-channel dark matter annihilation at NLO". In: *JHEP* 01 (2023), p. 157. DOI: 10.1007/JHEP01(2023)157. arXiv: 2211.06008 [hep-ph].

[35] Kalle Ala-Mattinen and Kimmo Kainulainen. "Precision calculations of dark matter relic abundance". In: *JCAP* 09 (2020), p. 040. DOI: 10.1088/1475-7516/2020/09/040. arXiv: 1912.02870 [hep-ph].

[36] Manuel Drees and Jie Gu. "Enhanced One-Loop Corrections to WIMP Annihilation and their Thermal Relic Density in the Coannihilation Region". In: *Phys. Rev. D* 87.6 (2013), p. 063524. DOI: 10.1103/PhysRevD.87.063524. arXiv: 1301.1350 [hep-ph].

[37] Simone Biondini et al. "Effective field theories for dark matter pairs in the early universe: cross sections and widths". In: *JHEP* 07 (2023), p. 006. DOI: 10.1007/JHEP07(2023)006. arXiv: 2304.00113 [hep-ph].

[38] Tobias Binder et al. "Non-Abelian electric field correlator at NLO for dark matter relic abundance and quarkonium transport". In: *JHEP* 01 (2022), p. 137. DOI: 10.1007/JHEP01(2022)137. arXiv: 2107.03945 [hep-ph].

[39] Martin Beneke, Francesco Dighera, and Andrzej Hryczuk. "Relic density computations at NLO: infrared finiteness and thermal correction". In: *JHEP* 10 (2014). [Erratum: JHEP 07, 106 (2016)], p. 045. DOI: 10.1007/JHEP10(2014)045. arXiv: 1409.3049 [hep-ph].

[40] Pritam Sen, D. Indumathi, and Debajyoti Choudhury. "Infrared finiteness of a complete theory of charged scalars and fermions at finite temperature". In: *Eur. Phys. J. C* 80.10 (2020), p. 972. DOI: 10.1140/epjc/s10052-020-08498-3.

[41] Pritam Sen, D. Indumathi, and Debajyoti Choudhury. "Infrared finiteness of a thermal theory of scalar electrodynamics to all orders". In: *Eur. Phys. J. C* 79.6 (2019), p. 532. DOI: 10.1140/epjc/s10052-019-7001-3. arXiv: 1812.04247 [hep-ph].

[42] G. Grammer Jr. and D. R. Yennie. "Improved treatment for the infrared divergence problem in quantum electrodynamics". In: *Phys. Rev. D* 8 (1973), pp. 4332–4344. DOI: 10.1103/PhysRevD.8.4332.

[43] D. R. Yennie, Steven C. Frautschi, and H. Suura. "The infrared divergence phenomena and high-energy processes". In: *Annals Phys.* 13 (1961), pp. 379–452. DOI: 10.1016/0003-4916(61)90151-8.

[44] D. Indumathi. "Cancellation of infrared divergences at finite temperature". In: *Annals Phys.* 263 (1998), pp. 310–339. DOI: 10.1006/aphy.1997.5758. arXiv: hep-ph/9607206.

[45] Martin Beneke, Francesco Dighera, and Andrzej Hryczuk. "Finite-temperature modification of heavy particle decay and dark matter annihilation". In: *JHEP* 09 (2016), p. 031. DOI: 10.1007/JHEP09(2016)031. arXiv: 1607.03910 [hep-ph].

[46] P. Sen P. Butola D. Indumathi. *Mathematica Notebooks for Dark Matter Annihilation Cross section at NLO.* https://www.imsc.res.in/~indu/Academic/DarkMatter/. Uploaded on 2024-04-20. 2024.

[47] Vladyslav Shtabovenko, Rolf Mertig, and Frederik Orellana. "FeynCalc 9.3: New features and improvements". In: *Comput. Phys. Commun.* 256 (2020), p. 107478. DOI: 10.1016/j.cpc.2020.107478. arXiv: 2001.04407 [hep-ph].

[48] Vladyslav Shtabovenko, Rolf Mertig, and Frederik Orellana. "New Developments in FeynCalc 9.0". In: *Comput. Phys. Commun.* 207 (2016), pp. 432–444. DOI: 10.1016/j.cpc.2016.06.008. arXiv: 1601.01167 [hep-ph].

[49] R. Mertig, M. Bohm, and Ansgar Denner. "FEYN CALC: Computer algebraic calculation of Feynman amplitudes". In: *Comput. Phys. Commun.* 64 (1991), pp. 345–359. DOI: 10.1016/0010-4655(91)90130-D.

[50] Wolfram Research, Inc. *Mathematica, Version 13.1.* Champaign, IL, 2022.

[51] R. L. Kobes and G. W. Semenoff. "Discontinuities of Green Functions in Field Theory at Finite Temperature and Density". In: *Nucl. Phys. B* 260 (1985), pp. 714–746. DOI: 10.1016/0550-3213(85)90056-2.

[52] Antti J. Niemi and Gordon W. Semenoff. "Thermodynamic Calculations in Relativistic Finite Temperature Quantum Field Theories". In: *Nucl. Phys. B* 230 (1984), pp. 181–221. DOI: 10.1016/0550-3213(84)90123-8.

[53] R. J. Rivers. *PATH INTEGRAL METHODS IN QUANTUM FIELD THEORY.* Cambridge Monographs on Mathematical Physics. Cambridge University Press, Oct. 1988. ISBN: 978-0-521-36870-4, 978-1-139-24186-1. DOI: 10.1017/CBO9780511564055.

[54] T. Altherr. "Introduction to thermal field theory". In: *Int. J. Mod. Phys. A* 8 (1993), pp. 5605–5628. DOI: 10.1142/S0217751X93002216. arXiv: hep-ph/9307277.

[55] Mathias Becker et al. *Dark matter freeze-in from non-equilibrium QFT: towards a consistent treatment of thermal effects.* Dec. 2023. arXiv: 2312.17246 [hep-ph].

[56] Ansgar Denner et al. "Feynman rules for fermion number violating interactions". In: *Nucl. Phys. B* 387 (1992), pp. 467–481. DOI: 10.1016/0550-3213(92)90169-C.